UNIVERSIDAD DE CHILE
FACULTAD DE CIENCIAS FÍSICAS Y MATEMÁTICAS
DEPARTAMENTO DE FÍSICA

PROSPECTS FOR CONSTRAINING NON-THERMAL ION ACCELERATION AND PROPAGATION IN SGR A* USING CTA

TESIS PARA OPTAR AL GRADO DE
MAGISTER EN CIENCIAS, MENCIÓN FÍSICA

CLAUDIO ALEJANDRO MUENA TOLEDO

PROFESOR GUÍA:
MARIO RIQUELME HERNÁNDEZ

PROFESOR CO-GUÍA:
ANDREAS REISENEGGER VON OEPEN

MIEMBROS DE LA COMISIÓN:
PABLO MOYA FUENTES
WALTER MAX-MOERBECK
CLAUDIO DIB VENTURELLI

Este trabajo ha contado con el apoyo parcial de los proyectos FONDECYT Proyectos regulares 1201582 (A.R.) y 1191673 (M.R.), y el Centro de Astrofísica y Tecnologías Asociadas (CATA; ANID Proyecto Basal FB210003).

SANTIAGO DE CHILE
2024

Perspectivas para limitar la aceleración y propagación de iones no-térmicos en Sgr A*, haciendo uso de CTA

Resumen

El espectro de la emisión difusa detectada en los centenares de parsecs interiores del Centro Galáctico sugiere la existencia de un acelerador central de rayos cósmicos capaz de energizar protones hasta energías de unos pocos PeV. Es sugerente asociar este PeVatrón con la fuente puntual de rayos gamma HESS J1745-290, que sin embargo muestra una ruptura espectral a unos pocos TeV, no mostrada por la emisión difusa. Esta tesis propone que ambas emisiones pueden explicarse por la misma población de rayos cósmicos inyectados con un espectro de ley de potencia hasta unos pocos PeV cerca del agujero negro supermasivo (SMBH) Sgr A*. En el modelo propuesto, la ruptura en el espectro de rayos gamma de la fuente puntual se debe a una transición dependiente de la energía en la forma en que los rayos cósmicos se difunden hacia el exterior desde las proximidades de Sgr A*, donde son inyectados, hasta $\sim 0,1$ pc del SMBH, donde se produce la mayor parte de la emisión. Esta transición depende de la relación entre el radio de Larmor de los CRs y la longitud de coherencia de la turbulencia magnética en el flujo de acreción. Por tanto, este estudio apoya la idea de que Sgr A* puede ser un PeVatron siempre que se cumplan algunas restricciones específicas sobre la estructura de la turbulencia magnética en el flujo de acreción de Sgr A*.

To my dear 'family show'

Table of content

List of Tables

List of Figures

Chapter 1

Introduction

This thesis is concerned with the open problem of the origin of cosmic rays (CRs) and their possible connection with the phenomenon of accretion onto black holes. The concept of ´cosmic ray´ refers to charged particles, principally protons, ions and electrons, which propagate with relativistic speeds through the Universe. Currently, the main goals in the study of CRs are to identify the sources where they are accelerated and understand the physical mechanisms that accelerate them. For CRs accelerated in the Milky Way (also called, ´galactic CRs´), one possible acceleration source is given by the shock fronts of supernova remnants (SNRs). In this process, known as diffusive shock acceleration (DSA), the charged particles repeatedly cross the shock front by continuously encountering magnetic inhomogeneities, so that they are successively reflected between the downstream and upstream regions of the shock front, gaining energy at each crossing. Although this process is relatively well understood, it is not yet clear whether SNRs can act as ´PeVatron´, capable of accelerating CRs up to PeV energies, as required by CRs detected on Earth.

The lack of conclusive observational verification has raised the question of whether other astrophysical systems may also contribute to the acceleration of CRs. In this thesis, we consider the possibility of accretion onto black holes as a possible CR source, focusing in particular on Sagittarius A* (Sgr A*), the super-massive black hole at the Galactic Center (GC), as an important CR acceleration source. Our study is motivated by the existence of the gamma-ray source HESS J1745-290, located in the GC, and whose origin has been speculated to be related to the CR acceleration phenomenon. We construct a gamma-ray emission model for HESS J1745-290 in which we assume that this source is powered by CRs injected in the immediate vicinity of Sgr A* and propagating outwards through the accretion flow. In this way, we constrain the propagation properties of CRs within the inner ~ 0.1 pc of the Galaxy so that these CRs can reproduce the spectral properties of HESS J1745-290.

This work is also motivated by the upcoming construction of world-class gamma-ray observatories in Chile and in the South American Andes, which will be able to study HESS J1745-290 and other gamma-ray sources with unprecedented accuracy in the next years.

1.1 The Galactic Center

The center of the Galaxy (inner $\sim$ 10 pc) is a region of considerable interest for the study of astrophysical phenomena. The presence of objects such as pulsar wind nebulae (PWNe), neutron stars, star clusters, SNRs, and the super-massive black hole Sgr A*, make this a very interesting region for the study of high-energy astrophysics. Surrounding the GC is the Central Molecular Zone (CMZ), a region whose extension is $\sim 300\,\mathrm{pc} \times 600$ pc [61], and which presents an important brightness in radio emission. In the inner part of the CMZ, $r \leq 50$ pc, is the Sgr A radio emission structure (see Fig. 1.1), composed by the compact Sgr A* radio emission source, coincident in location with the central supermassive black hole, the Sgr A East SNR, and the triple spiral structure of dust and gas Sgr A West, which is surrounded by a torus of molecular gas known as the circumnuclear disk [61].

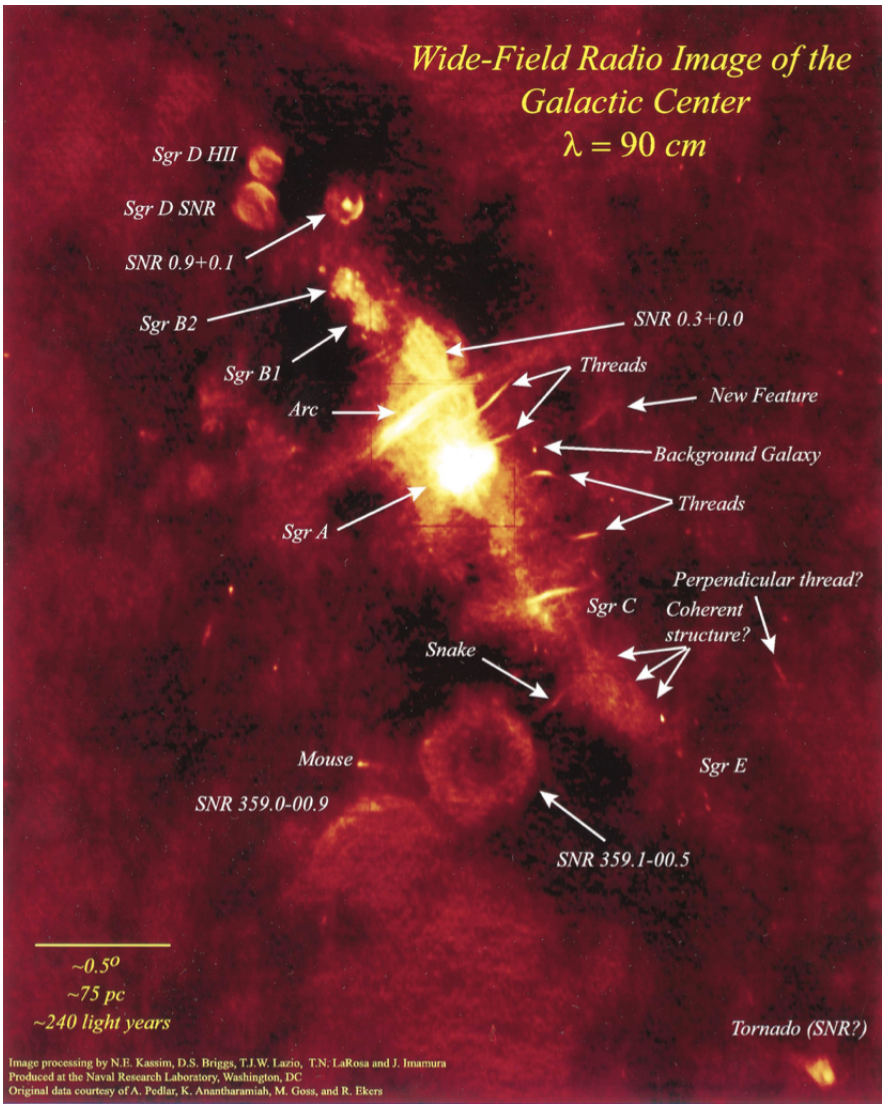

Figure 1.1 Long-wavelength ($\lambda = 90$ cm) VLA image of the Central Molecular Zone [38].

1.2 Gamma-ray observations

One way to increase our knowledge about this region is through the detection of gamma rays originating from the aforementioned astrophysical objects. Part of these gamma rays can be classified into: high-energy (HE) gamma-rays and very-high-energy (VHE) gamma-rays, corresponding to $30\,\text{MeV} \lesssim E_\gamma \lesssim 30$ GeV, and to $30\,\text{GeV} \lesssim E_\gamma \lesssim 30$ TeV [26], respectively. The HE range is studied by space telescopes, such as the International Laboratory for Gamma Ray Astrophysics (INTEGRAL, launched in 2002), the Astro-Rivelatore Gamma a Immagini Leggero (AGILE, launched in 2007) and the Fermi Large Area Telescope (Fermi LAT, launched in 2008). These telescopes have discovered various sources of gamma-rays near the Galactic Center. An interesting detection by Fermi LAT is the point source 1FGL J1745.6-2900, whose location at the center of the Galaxy spatially coincides with the point-like VHE gamma-ray source HESS J1745-290. Although these sources have been extensively studied [61], their nature and possible common origin is not yet clear.

For the VHE range, observations have been made mainly by ground-based telescopes such as the Imaging Atmospheric Cherenkov Atmospheric Telescopes (IACTs) and water Cherenkov detectors. Both types of observatories are capable measuring the energies and directions of propagation of VHE gamma-rays through the showers of charged relativistic particles they produce in the Earth's atmosphere.

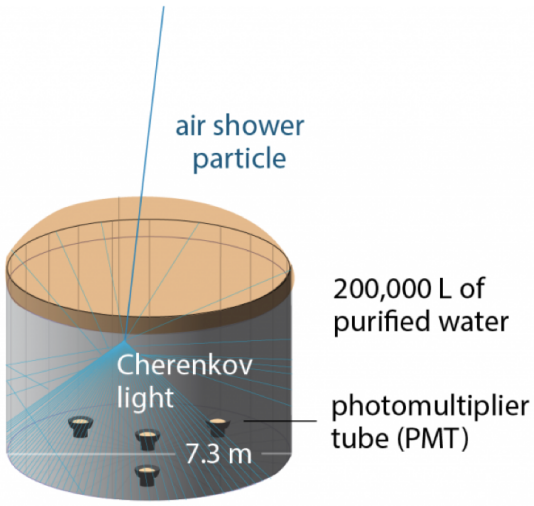

Figure 1.2 Example of a gamma ray detection scheme for a water Cherenkov detector (HAWC [45]).

The water Cherenkov detectors measure the Cherenkov radiation[1] produced by the shower particles as they propagate through a volume of water (see Figure 1.2). These observatories operate continuously (nearly 100% duty cycle), detecting VHE gamma rays coming from a large fraction of the sky, however, their angular resolution is lower compared to IACTs. The main currently operating water Cherenkov observatories are the High-Altitude Water

[1]Cherenkov radiation corresponds to electromagnetic radiation produced by charged particles whose velocities are greater than the speed of light in the medium in which they propagate.

Cherenkov gamma-ray observatory (HAWC) and the Large-High Altitude Air Shower Observatory (LHAASO).

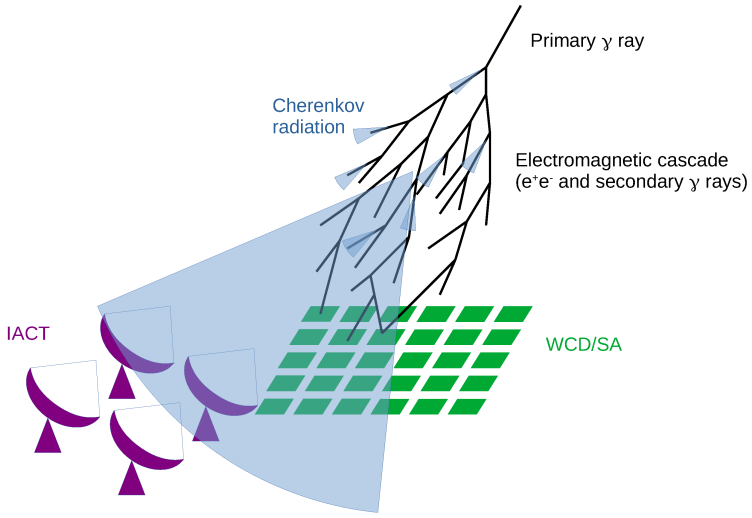

Figure 1.3 Gamma ray detection scheme for IACTs [55].

The IACTs detect Cherenkov radiation emitted in the atmosphere by the shower of particles propagating in it (see figure 1.3). This type of observatory observes only during dark nights and have a limited field of view, so they must point to the specific sources to be studied. On the other hand, they have a higher angular resolution. There are currently three main IACTs in operation: the Major Atmospheric Gamma-ray Imaging Cherenkov Telescope (MAGIC) in La Palma (Spain) [37], the Very Energetic Radiation Imaging Telescope Array System (VERITAS) in Arizona (USA) [50], and the High Energy Stereoscopic System (H.E.S.S.) in Namibia [1]. Due to its location in the Southern Hemisphere, H.E.S.S. has been the most suitable for studying the inner Galaxy in the VHE range. In fact, observations by H.E.S.S. led to the detection of the aforementioned point-like gamma-ray source HESS J1745-290 (See Fig. 1.4).

Added to these observatories, an upcoming IACT, the Cherenkov Telescope Array Observatory (CTAO), will be put into operation in the coming years. This observatory consists of two IACT arrays, one located in the Northern Hemisphere, specifically at La Palma, in the Canary Islands, Spain (CTA North), and the other located in the Southern Hemisphere, at Paranal in the Antofagasta region, Chile (CTA South). The upcoming observatory will greatly improve the angular resolution and sensitivity of current IACTs. An interesting point, and potentially important for the development of national high-energy astronomy and astrophysics, is that its location in the Atacama desert is ideal for observing the Galactic Center, considering that this will be the most important VHE gamma ray observatory on Earth. Motivated by this, the goal of the present thesis is to build a model for the emission of gamma-rays produced by CRs potentially accelerated in the accretion process onto Sgr A*. CTA South will provide us with a perfect opportunity to test this model, shedding light on its possible connection with the central source HESS J1745-290.

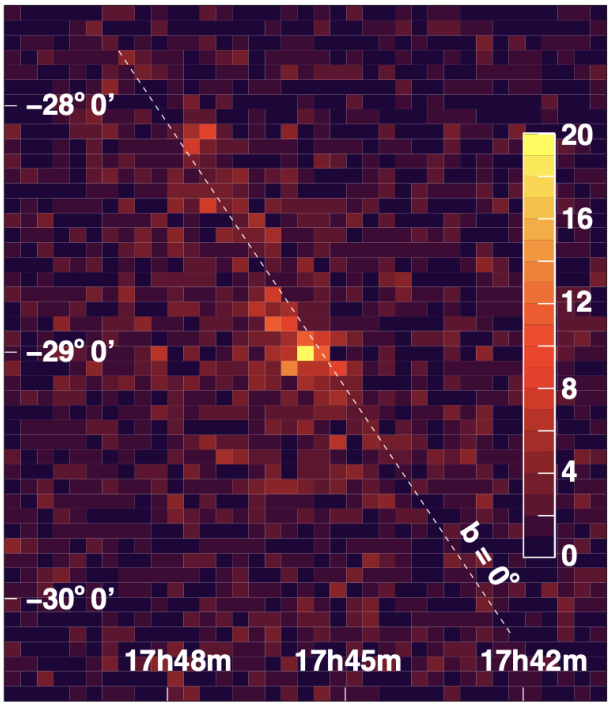

Figure 1.4 Gamma-ray excess in the Galactic Center (inner $\sim$ 10 pc), detected by H.E.S.S. [6].

1.3 The origin of HESS J1745-290

There are many astrophysical phenomena in which HE and VHE gamma-rays can be produced. However, the 3 arcmin angular resolution of the current gamma-ray observatories, equivalent to $\sim$ 10 pc in projected distance from the Galactic Center, makes it difficult to associate a gamma-ray source, like the point-like VHE gamma-ray source HESS J1745-290, with a particular astrophysical system in that region. Three main candidates have been proposed for HESS J1745-290: (1) annihilation of dark matter particles in the density peak at the Galactic Center [14], (2) the PWN G359.95-0.04 [62] and (3) a CR acceleration process associated with the accretion of plasma onto the central black hole Sgr A* [2]. In scenario (1), dark matter particles and antiparticles collide, annihilating each other and giving rise to VHE gamma-rays [32]. In scenario (2), relativistic electrons and positrons within the PWN scatter ambient photons up to the gamma-ray range. This process is called inverse compton scattering (ICS) and constitutes a ubiquitous process for gamma-ray emission in astrophysics. In scenario (3), CRs (electrons and ions) accelerated in the vicinity of Sgr A* and propagating outwards through the inflowing plasma (here and hereinafter referred to as 'gas') can contribute to the gamma-ray emission. While electrons produce gamma-rays by ICS, ions (mainly protons) are injected into the surrounding medium and collide with background protons producing neutral pions which decay into VHE gamma-photons. This process, usually called ´hadronic´ gamma-ray emission, takes place during the transport of CRs in the interstellar medium (ISM), where inelastic collisions between relativistic charged particles and atomic nuclei (e.g., H^+) present in the background gas of the ISM would occur. The interaction between these particles produces new particles. In the case of proton CRs, if their energy is $E \gtrsim 280$ MeV [26], the collision can produce secondary particles, like charged

pions, π^- and π^+, and neutral pions π^0. These particles decay in a relatively short time ($t \sim 10^{-8}$ s and $\sim 10^{-16}$ s, for charged and neutral pions respectively) producing in turn another series of new particles such as electrons, muons, neutrinos, and gamma-ray photons. Through the study of these particles it is possible to obtain indirect information regarding the parent CRs. In particular, one can show that the energy-spectrum of the parental CRs looks very similar to energy-spectrum of the emitted gamma-ray photons, showing essentially the same spectral index but with a correspondence between the CR energy (E) and the gamma-ray energy (E_γ) given by

$$E_\gamma \sim 0.1E. \tag{1.1}$$

These relations provide a very simple and useful tool to infer the properties of the CRs from the spectrum of gamma-rays produced by a hadronic process.

1.4 Sgr A* as a ´PeVatron´

The scenario of HESS J1745-290 being produced by the hadronic emission driven by ions being accelerated by Sgr A* is supported by the diffuse gamma-ray emission detected from the CMZ. Observations made by H.E.S.S. towards the CMZ revealed in 2016 [2] diffuse emission of very-high-energy gamma-rays over an extension of $\sim$ 300 pc (see Fig. 1.5). The spatial distribution of this emission source has suggested the presence of VHE CRs ($\sim$ PeV) injected from the Galactic Center, assuming that gamma rays are mainly produced by the collision of hadronic CRs with the background gas present in the CMZ. The radial profile of the energy density of CRs, deduced from the gamma-ray emission and the high gas density distribution, suggests a high density of CRs in the CMZ compared to the Galactic CR population, which supports the hypothesis of a central accelerator. Another plausible assumption for this diffuse emission is a leptonic origin by Inverse Compton occurring in the CMZ. However, the large size of the diffuse source would imply important radiative losses for the relativistic electrons during their propagation disfavoring this scenario (see 'Methods' on [2]). In the hadronic scenario, the diffuse emission requires an accelerator of CRs up to $\sim$ PeV energies, an object known as PeVatron, which seems to be coincident with the point-like source
HESS J1745-290. Interestingly, the spectral energy distribution of the diffuse emission and the point emission are practically the same, except that the spectrum of the point-like emission presents a break at energies $E_\gamma \sim 3$ TeV. Despite this, the spectral match together with the spatial match of the possible accelerator and HESS J1745-290, strongly suggest a common origin for these two emissions.

In this scenario, the presence of a spectral break in HESS J1745-290, absent in the diffuse emission, needs an explanation. For this various suggestions have been made: **(1)** attenuation of VHE gamma-rays ($\gtrsim$ 10 TeV) through their interaction with infrared photons of the interstellar radiation field in the GC [31]. In this scenario, a clumpy structure of the interstellar medium in the GC would enhance the absorption by interstellar radiation of the most energetic gamma photons in the VHE range. According to this model, this absorption would not be present for the gamma photons of the diffuse emission in the CMZ. **(2)** A decrease in the power of CR injection [40]. In this scenario, the diffuse emission would be associated with VHE protons (up to $\geq$ 1 PeV) injected by Sgr A* in the past, while the point-

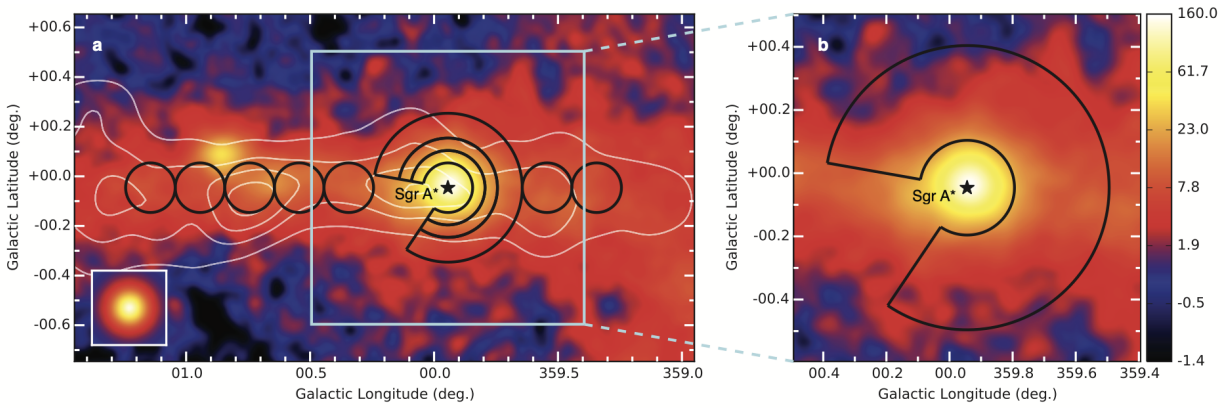

Figure 1.5 VHE gamma-rays in the inner 300 pc of the Galaxy [2]. The left panel shows the gamma-ray emission in the CMZ, and the right panel shows gamma-ray emission in the inner ~ 70 pc of the CMZ.

like source would be associated with recently injected, lower-energy CRs. This reduction in injection would result in a break in the spectrum for the point-like source.

1.5 Our model

In this thesis, we propose an alternative scenario to explain the discrepancy between the point-like source and the diffuse emission, based on the properties of CR diffusion within the emission region of HESS J1745-290. The spectral energy distribution of HESS J1745-290 can be explained by VHE CRs injected by Sgr A* that subsequently interact with the black hole accretion flow [49]. The accretion flow is mainly fuelled by the wind from Wolf-Rayet stars [20] orbiting at $\sim 0.1 - 1$ pc from Sgr A*. In recent simulations [21, 49] of the Sgr A* accretion flow gas is turbulently injected by stellar winds, outwards and into the accretion flow, and only a small fraction of this gas ends up being accreted onto the black hole. In our proposed scenario, the injected CRs have a time-independent power-law energy spectrum that reaches $\sim$ PeV energies, which is the same as needed to explain the diffuse emission from the CMZ. In order to reconcile the spectral break of HESS J1745-290 with its absence in the diffuse emission, we invoke an energy-dependent transition for the CR diffusion coefficient within the accretion flow. This change in the diffusive transport of CRs would not be present in the CMZ, explaining the lack of a break in its spectral energy distribution.

CR diffusion through turbulent magnetic fields can take different qualitative forms, depending on the energy of the CR, the intensity of the magnetic field, and the properties of the turbulence present in the region [64]. In fact, it has been pointed out that the propagation of charged particles in environments with strong, isotropic magnetic turbulence, depends on the relationship between the Larmor radius R_L and the magnetic turbulence coherence length l_c [27, 57], which is the spatial scale at which most of the magnetic turbulence energy is injected. These studies have found two main diffusion regimes, depending on whether R_L is larger or smaller than l_c. In simulations of test particles [43] these two diffusion regimes are clearly appreciated. We will show that the transition between these regimes can account for

the observed break in the spectrum of HESS J1745-290.

In this thesis we develop a model for the point-like gamma-ray source HESS J1745-290, estimating the gamma-ray flux coming from the inner parsec of the GC. Assuming certain characteristics of the Sgr A* accretion flow environment (gas density and magnetic field profile), we solve the CR transport equation (Eqs. 2.7 and 2.8) to analytically obtain the CR density distribution in the Sgr A* accretion flow, after imposing certain continuity conditions between the different transport regimes (see Fig. 3.1).Once the density of CRs is obtained, considering the gas density profile obtained in the simulations of Ressler et al. 2018 [49], and assuming a characteristic cross section for this inelastic collisions between CRs and background protons (of the Sgr a* accretion flow)[26], we estimate the total gamma-ray flux produced in the central parsec of the GC. In this way, we will compare the gamma-ray flux obtained with the observations made by H.E.S.S. [19], limiting ourselves to adjust our free parameters respecting the current observational constraints (see section 4). After fitting our model with the H.E.S.S. observations, our results suggest strong constraints for the structure of the magnetic turbulence present in the Sgr A* accretion flow and a broken power law like-shape of the spectral energy distribution of HESS J1745-290.

Our model favors Sgr A* as the source of CR acceleration [9], and indeed proposes Sgr A* as a plausible ´PeVatron´ candidate, i.e., as a source of CRs up to PeV energies.

Thus, the relevance of this thesis is to help clarify the possible contribution of the accretion onto Sgr A* (and onto black holes in general) in the phenomenon of CR acceleration. As will be explained below, the results of this thesis will be testable by the future generation of ground-based gamma-ray telescopes, like the Cherenkov Telescope Array Observatory (CTAO [59]) and the Southern Wide-field Gamma-ray Observatory (SWGO [34]), soon to be built in Chile and in the South American Andes, respectively.

Chapter 2

Model components

The development of a model for the high-energy gamma-ray emission associated with the transport of CRs in the Sgr A* accretion flow requires characterizing the CR density distribution in the accretion flow and their interaction with the background gas. To this end, in this chapter we describe the following four main components of our model, emphasizing the assumptions made for each of them: (1) the gas properties and magnetic turbulence of the Sgr A* accretion flow, (2) the modeling of the injection of CRs into the Sgr A* accretion flow, (3) the characterization of the CR transport through the Sgr A* accretion flow, where we assume that both diffusion and advection contribute to CR propagation, and (4) the mechanism of high-energy gamma-ray emission of hadronic origin.

2.1 Accretion flow properties

Due to the low luminosity of Sgr A*, $L \sim 10^{-9} L_{\rm Edd}$ (where $L_{\rm Edd}$ corresponds to the Eddington luminosity, [16]), the accretion flow around the supermassive black hole is characterized as a Radiatively Inefficient Accretion Flow (RIAF). According to observations at the Galactic Center, presumably this accretion flow is mainly fed by the wind of a few tens of Wolf-Rayet type stars orbiting around Sgr A* at a radius $r \sim 0.1 - 1$ pc [20].

In order to characterize the physical properties of the gas in the Sgr A* accretion flow, we use the hydrodynamic and MHD simulations of the Sgr A* accretion flow, which show similar results [48, 49]. These simulations are able to reproduce the total X-ray luminosity observed by Chandra [11], the radial gas density profile in the inner part of the Sgr A* accretion flow ($\gtrsim 10^{-4}$ pc) constrained by X-ray observations [30], and the constrained value of the accretion rate near the supermassive black hole $\dot{M} \sim 10^{-8}\, M_{\odot}$/year [41, 54]. In the numerical simulations of Ressler et al. 2018 [49], four regions are identified within the accretion flow:

i) Region I: an inflow-dominated region at distances $r \lesssim 0.01$ pc, where the mass accretion rate is roughly constant.

ii) Region II: a 'stagnation' region at 0.01pc $\lesssim r \lesssim 0.07$ pc, where the net mass accretion rate, due to inflows and outflows of the gas, can be considered approximately null.

iii) Region III: Located at $0.07\,\mathrm{pc} \lesssim r \lesssim 0.4$ pc, this region is called the 'feeding' region. This is where most of the gas injection from the Wolf-Rayet winds occurs. In this region (and in region IV) gas motions are predominantly away from the GC.

iv) Region IV: Defined by $r \gtrsim 0.4$ pc, this region is dominated by gas outflows and expands at essentially the speed of the Wolf-Rayet winds.

From these simulations, we also note that the background gas density in the accretion flow behaves as two power laws in the radius r (see Fig. 11 in [49]) such that

$$n_g(r) \approx \begin{cases} 25 \left(\frac{r}{0.4\mathrm{pc}}\right)^{-1} \mathrm{cm}^{-3} & \text{for } r \leq 0.4\,\mathrm{pc}, \\ 25 \left(\frac{r}{0.4\mathrm{pc}}\right)^{-2} \mathrm{cm}^{-3} & \text{for } r > 0.4\,\mathrm{pc}, \end{cases} \tag{2.1}$$

which means that for regions I, II and III the gas density in the RIAF scales as $\sim r^{-1}$, whereas in region IV it scales as $\sim r^{-2}$.

On the other hand, based on Figure 5 of Ressler et al. 2020 [48], we approximate the rms magnetic field in the accretion flow as a power-law

$$B(r) \approx 10\,\hat{B} \left(\frac{r}{10R_g}\right)^{-n} \mathrm{G}, \tag{2.2}$$

where n and $\hat{B}$ are free parameters. According to the same simulations, $n \approx 1 - 0.9$, while $\hat{B}$ is a factor of order unity, quite independent of the conditions assumed for the wind of Wolf-Rayet stars. In contrast to the magnetic field, the value of the coherence length l_c in the accretion flow is very uncertain. For this, we also assume a power-law shape,

$$l_c(r) \approx 10^{14}\,\hat{l}_c \left(\frac{r}{0.07\mathrm{pc}}\right)^{m} \mathrm{cm}, \tag{2.3}$$

where $\hat{l}_c$ and m represent free parameters in our model.

2.2 CR injection

We assume that all the CRs that exist in the inner region of the Galactic Center GC, $r \lesssim 1$ pc, have been injected from the region close the black hole at radii $r \gtrsim R_g$ (with $R_g = 2GM_{BH}/c^2$ corresponding to the gravitational radius of the super-massive black hole) outward, by some acceleration mechanism occurring on these scales. Although it is known that DSA process [27], magnetic reconnection or other process could accelerate particles in accretion disks [22], the underlying mechanism which accelerates the CRs in the Sgr A* accretion flow is beyond the scope of this thesis. Therefore, we limit ourselves to assume a stationary and spherically symmetric CR density distribution, where the CRs are ultra-relativistic protons continuously injected in the vicinity of Sgr A* and propagating radially through its accretion flow.

We model the number of injected CRs per unit energy E and per unit time t, for CR energies larger than 1 TeV, as a power-law given by

$$\frac{dN}{dEdt}(E) = 2.3 \times 10^{36} \left(\frac{E}{1\,\mathrm{TeV}}\right)^{-q} f(q, E_{max})\, \hat{Q}\, \mathrm{erg}^{-1}\mathrm{s}^{-1}, \tag{2.4}$$

for $E < E_{max}$ ($dN(E)/dEdt = 0$ otherwise). In Eq. 2.4, q is the spectral index of the injected CR spectrum, $\hat{Q}$ is an order unity parameter that quantifies the injection power, and

$$f(q, E_{max}) = \frac{2-q}{\left(\frac{E_{max}}{1\,\mathrm{TeV}}\right)^{2-q} - 10^{2-q}}. \tag{2.5}$$

Eq. 2.5 implies that the CR injection power for $E \geq 10$ TeV, $Q(E)$, is given by

$$Q(E > 10\mathrm{TeV}) \approx 6 \times 10^{36} \hat{Q} \mathrm{erg\ s}^{-1}. \tag{2.6}$$

With these assumptions, the three free parameters that characterize CR injection are q, $\hat{Q}$ and E_{max}.

2.3 CR transport

In our model, we assume that both diffusion and advection contribute to CR propagation. As we see below, advection is the dominant process at $r \gtrsim 0.07$ pc for low enough CR energies, while for $r \lesssim 0.07$ pc, diffusion dominates for all energies of interest, that is for $1\mathrm{TeV} \leq E \leq E_{max}$. Thus, as an approximation, in our calculations we impose that CRs are transported either by diffusion or advection, depending on which process is more efficient at a given energy E and distance r from Sgr A*.

We consider our model to be stationary, such that, neglecting reabsorption processes and assuming that CRs do not lose energy, the number of CRs passing through a spherical shell of radius r per unit time and energy is independent of r, and it is only determined by their injection rate (Eq. 2.4). This implies that in the diffusive regime

$$\frac{dN}{dEdt}(E) = -4\pi r^2 D(E, r) \frac{\partial}{\partial r}\left(\frac{dn_{CR}(E, r)}{dE}\right), \tag{2.7}$$

where $D(E, r)$ is the CR diffusion coefficient and $dn_{CR}/dE(E, r)$ is the CR density per unit energy, which is the quantity that we need to calculate in order to subsequently calculate the gamma-ray emission.

On the other hand, in the cases in which advection dominates, CR transport is determined by the average background gas velocity along the radial direction, $v_{\rm gas}(r)$. In that case,

$$\frac{dN}{dEdt}(E) = 4\pi r^2\, v_{\rm gas}(r)\, \frac{dn_{\rm CR}}{dE}(E, r). \tag{2.8}$$

Notice that advective transport could also be due to turbulent motions of the gas, which may give rise to turbulent diffusion. We show below that this effect can be neglected for the cases of interest, so in our model CR transport is determined by the properties of $D(E, r)$ and $v_{\rm gas}(r)$. In particular, given Eqs. 2.7 and 2.8, we decide whether diffusion or advection is the dominant process by defining a diffusion velocity $v_{\rm diff}$ as

$$v_{\rm diff}(E, r) \equiv D(r, E)/r, \tag{2.9}$$

and determining whether $v_{\rm diff}(E, r)$ is larger or smaller than $v_{\rm gas}(r)$, respectively. Once one of these two velocities is found to dominate, as an approximation we assume the transport to be provided only by that velocity, which allows us to have a reasonable estimate for $dn_{CR}/dE(E, r)$. In what follows, we describe the assumptions made in order to obtain $D(E, r)$ and $v_{\rm gas}(r)$.

2.3.1 CR diffusion

Since magnetic fields in astrophysical media are usually highly turbulent [27], CRs propagate principally in a diffusive manner. In this sense, while different approaches have been established to describe the propagation of CRs in turbulent media ([35, 42, 53]), where the magnetic field is assumed to be the addition of a constant background field with small perturbations, other studies, such as Subedi et al. 2017 [57], propose that in environments with isotropic magnetic turbulence, the magnetic field can be modeled simply by means of random magnetic inhomogeneities. In this case, the transport of CRs is characterized by the spatial scale of the magnetic turbulence, which determines the ability of the magnetic field to deflect the trajectory of the charged particle. This spatial scale is given by the coherence length l_c, understanding it as a distance over which the magnetic field lines are correlated. Another important parameter is the Larmor radius ($R_L = E/eB$, where e is the proton electric charge and B is the magnitude of the magnetic field), which is the radius of gyration of the charged particle around the probed magnetic field lines. Subedi et al. [57] pointed out that two main diffusion regimes emerge depending of the relation between R_L and l_c. If $R_L \gg l_c$, the CR will probe many deviations from the magnetic field lines, randomly deflecting its approximately rectilinear path, diffusing in space as it propagates. This situation is identified as high-energy diffusion regime. On the contrary, if $l_c \gg R_L$, the CR will perceive a ´local´, mainly coherent, magnetic field, making a large number of turns around the field lines before they will be uncorrelated. We refer to this regime as low-energy diffusion regime. Fig. 2.1 shows different test particle simulations that quantify these two diffusion regimes through the mean free path λ_{mfp} (normalized by l_c) of the CRs.

The main aspects to be considered for the modeling of CR transport in an isotropic magnetic turbulence medium in the high and low-energy diffusion regimes are presented below, deriving, in first order approximations, the expressions for the mean free path consistent with theoretical results [27, 57] and test particle simulation results [43].

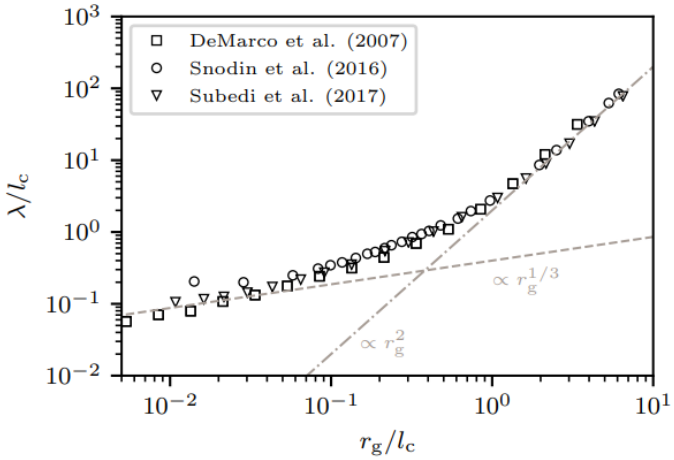

Figure 2.1 Mean free path λ as a function of the Larmor radius r_g (both normalized by the coherence length l_c, where $r_g = R_L$ in our notation), computed from test particle simulations [43].

Low-Energy Diffusive regime

This regime appears when $R_L \ll l_c$. On scales $\lesssim l_c$ the magnetic field can be written as $\mathbf{B} \approx B_0\hat{z} + \delta\mathbf{B}(\mathbf{r})$, where B_0 and $\hat{z}$ are the magnitude and direction of the mean magnetic field over a volume of size $\sim l_c$, and $\delta\mathbf{B}(\mathbf{r})$ is a random inhomogeneity of the magnetic field, such that $\delta B \ll B_0$. As a first approximation, the trajectory of a CR will be mainly helical, such that its velocity in the z direction is

$$v_z = \mu\, v_{CR} \qquad (\mu = cos\theta) \tag{2.10}$$

where θ is the pitch-angle, and $\mathbf{v}_{CR}$ is the velocity of the CR.

The projection of the velocity on a plane perpendicular to the mean magnetic field direction $\hat{z}$ satisfies

$$\frac{d\mathbf{v}_\perp}{dt} = \frac{\Omega}{B_0}\mathbf{v}_\perp \times \mathbf{B}_0 \tag{2.11}$$

where $\Omega = eB_0/(\gamma mc)$ is the frequency of the CR gyro-motion. The parallel component of the velocity changes due to the random magnetic inhomogeneities (see Figure 2.2), such that

$$\frac{dv_z}{dt} = \frac{\Omega}{B_0}\mathbf{v}_\perp \times \delta\mathbf{B} \cdot \hat{z}. \tag{2.12}$$

In one turn around the mean magnetic field the displacement along the field lines is

$$\triangle z = \frac{2\pi v_z}{\Omega} = 2\pi R_L \mu, \tag{2.13}$$

where $R_L = v_{CR}/\Omega$ is the Larmor radius. Defining a wave-number $k^* \sim 1/R_L\mu$ for some random magnetic inhomogeneinity δB^* in a scale $\triangle z^* \approx 2\pi/k^*$, the CR parallel velocity v_z

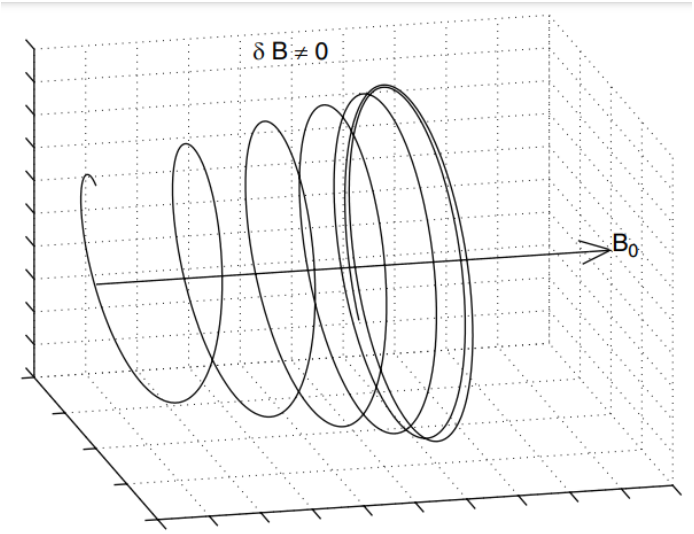

Figure 2.2 CR parallel diffusion representation [53].

will vary as

$$|\triangle v_z| \approx \triangle t \frac{\Omega}{B_0} |\mathbf{v}_\perp||\delta \mathbf{B}^*| \sim v_\perp \frac{\delta B^*}{B_0}, \tag{2.14}$$

where $\triangle t \approx 2\pi/\Omega$.

These variations are random, so v_z will change substantially after the CR has traveled a distance

$$\lambda_{mfp} \sim \triangle z^* \left(\frac{v_z}{\triangle v_z}\right)^2 \sim R_L \mu \left(\frac{v_z}{v_\perp}\right)^2 \left(\frac{B_0}{\delta B^*}\right)^2. \tag{2.15}$$

Assuming a randomly oriented velocity vector, we take $v_z \sim v_\perp$, so

$$\lambda_{mfp} \sim R_L \left(\frac{B_0}{\delta B^*}\right)^2. \tag{2.16}$$

In Kolmogorov turbulence, the energy density per unit wave number k is $u(k) \propto k^{-5/3}$, therefore the energy contained in eddies of size $\sim k^{-1}$ is $ku(k) \sim k^{-2/3}$. Noting that the energy contained in eddies of sizes $\sim l_c$ and R_L are proportional to B_0^2 and δB^{*2}, respectively, one can note that

$$\frac{\delta B^*}{B_0} \sim \left(\frac{l_c}{R_L}\right)^{-1/3}, \tag{2.17}$$

and thus

$$\lambda_{mfp} \sim R_L \left(\frac{l_c}{R_L}\right)^{2/3} = R_L^{1/3} l_c^{2/3}. \tag{2.18}$$

This ´one-dimensional´ mean free path, is defined for scales $\lesssim l_c$. The time t_c taken by the CR to traverse a step of size l_c is given by

$$\frac{l_c^2}{t_c} \sim \lambda_{mfp}\, c. \tag{2.19}$$

Therefore, considering that in spatial scales $\gg l_c$ the CRs will undergo random 3-dimensional steps of size $\sim l_c$ in times $\sim t_c$, one can estimate the isotropic, 3D diffusion coefficient as

$$D \sim \frac{l_c^2}{t_c} \sim c\, R_L^{1/3} l_c^{2/3}. \tag{2.20}$$

High-Energy Diffusive regime

This regime appears when $R_L \gg l_c$. Since the magnetic field is coherent on a scale l_c, the direction of motion of the CRs will change by an angle $\theta_1 \sim l_c/R_L$ in a random direction as they travel this distance (see Fig. 2.3).

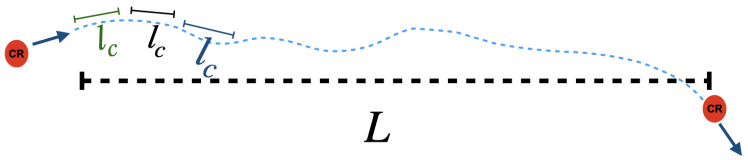

Figure 2.3 Scheme for the transport of a cosmic-ray in the High-Energy Diffusive regime

Thus, the deflection angle θ_n over n steps of size l_c satisfies

$$\langle \theta_n^2 \rangle \approx n\, \theta_1^2 \sim (L/l_c)(l_c/R_L)^2 \tag{2.21}$$

where $L = n l_c$ is the total distance traveled. The mean free path corresponds to a distance $\lambda_{mfp} = L$ for which $\langle \theta_n^2 \rangle \sim 1$, therefore

$$\lambda_{mfp} \sim \frac{R_L^2}{l_c}. \tag{2.22}$$

CR diffusion in the Sgr A* accretion flow

We assume that the MHD turbulence through which the CRs propagate in the Sgr A* accretion flow has a vanishing mean magnetic field and is characterized by a Kolmogorov spectrum with a coherence length l_c (see Eq. 2.3). From Figure 2.1 we can read that, for $R_L \ll l_c$,

$$\lambda_{\rm mfp} \approx 0.4\, l_c^{2/3} R_L^{1/3}, \tag{2.23}$$

while, for $R_L \gg l_c$,

$$\lambda_{\rm mfp} \approx 2\, l_c^{-1} R_L^2, \tag{2.24}$$

with a smooth transition for $R_L \sim l_c$. As an approximation for this transition, we simply take

$$\lambda_{\rm mfp} = \begin{cases} 0.4\, l_c^{2/3} R_L^{1/3} & \text{for} \quad R_L \leq 0.38\, l_c, \\ 2\, l_c^{-1} R_L^2 & \text{for} \quad R_L > 0.38\, l_c. \end{cases} \tag{2.25}$$

Considering Eqs. 2.23 and 2.24 for the spatial dependence of B and l_c, we find that, for the case where $R_L \ll l_c$ the diffusion coefficient is given by [27]

$$\begin{aligned} D(E,r) &= \frac{\lambda_{mfp}(E,r)\, c}{3} = \frac{0.4\, c\, l_c(r)^{2/3} R_L(E,r)^{1/3}}{3} \\ &= 6\times 10^{21} (2.1\times 10^4)^{-2m/3}\, {\rm cm}^{-2}{\rm s}^{-1} \left(\frac{E}{1{\rm TeV}}\right)^{1/3} \left(\frac{r}{10 R_g}\right)^{\frac{1}{3}(n+2m)} \hat{B}^{-1/3} \hat{l}_c^{2/3}. \end{aligned} \tag{2.26}$$

On the contrary, for the cases where $R_L \gg l_c$ the diffusion coefficient is given by

$$\begin{aligned} D(E,r) &= \frac{\lambda_{mfp}(E,r)\, c}{3} = \frac{2\, c\, l_c(r)^{-1} R_L(E,r)^2}{3} \\ &= 2\times 10^{13} (2.1\times 10^4)^{m}\, {\rm cm}^{-2}{\rm s}^{-1} \left(\frac{E}{1{\rm TeV}}\right)^{2} \left(\frac{r}{10 R_g}\right)^{2(n-m/2)} \hat{B}^{-2} \hat{l}_c^{-1}. \end{aligned} \tag{2.27}$$

2.3.2 CR advection

In the cases in which advection dominates, CR transport is determined by the average background gas velocity in the radial direction, $v_{\rm gas}(r)$. Thus, in order to model $v_{\rm gas}(r)$, we use the results of hydrodynamic and MHD simulations of Ressler et al. 2017, 2020 [49, 48], in which the kinematic of the gas is characterize in the four regions described in Section 2.1. In region I, we consider a mass accretion rate for Sgr A* of $3\times 10^{-8} M_\odot/$ year [48], with which we find that in this region the radial velocity $v_{\rm gas}$ is

$$v_{\rm gas}(r) = -\frac{\dot{M}}{4\pi r^2 n_g(r) m_p} \approx -10^5 \left(\frac{r}{0.01{\rm pc}}\right)^{-1} {\rm cm/s}. \tag{2.28}$$

In region II, the average radial velocity of the gas tends to cancel out, therefore CR transport should not be significantly affected by this velocity in this region. In what follows,

we neglect the effect of $v_{\rm gas}(r)$ for regions I and II, for which we assume that CR transport is dominated by diffusion. The validity of this assumption is verified in Chapter 4.

In regions III and IV ($r > 0.07$ pc), we can estimate the gas velocity $v_{\rm gas}$ using the results of [49], where it is shown that

$$v_{\rm gas} \approx \begin{cases} 700(r/0.4{\rm pc})\ {\rm km/s} & \text{for } 0.07\ {\rm pc} < r < 0.4\ {\rm pc} \\ 700\ {\rm km/s} & \text{for } r > 0.4\ {\rm pc}. \end{cases} \tag{2.29}$$

2.4 Hadronic emission

The hadronic emission comes from the decay of neutral pions produced in the collision of CRs with the Sgr A* accretion flow background gas.

Let σ_{pp} be the cross-section for the collision between high-energy protons (CRs) and low-energy protons (background gas), thus the number of pions N_{π^0} produced per unit energy, time and volume, is given [26] by

$$\frac{dq_{\pi^0}}{dE_{\pi^0}} = n_H\, c \int dE\, \frac{d\sigma_{pp}}{dE_{\pi^0}}(E, E_{\pi^0})\, \frac{dn_{CR}}{dE} \tag{2.30}$$

where $q_{\pi^0} = dN_{\pi^0}/dtdV$, n_H is the gas density, n_{CR} the CR density, and c the speed of light, which represents the velocity of the CRs in the ultra-relativistic case, and where the expression for the cross-section σ_{pp} can be estimated from experimental data. A common approximation [26] is

$$\frac{d\sigma_{pp}}{dE_{\pi^0}}(E, E_{\pi^0}) \approx \delta(E_{\pi^0} - \kappa_\pi E)\sigma_{pp}(E), \tag{2.31}$$

which is known as the δ-approximation, where $\kappa_\pi \approx 0.17$ is the mean fraction of the kinetic energy of the CR transferred to the pion π^0 in the collision. With this approximation, one obtains

$$\frac{dq_{\pi^0}}{dE_{\pi^0}} \approx \frac{c\, n_H}{\kappa_\pi}\, \sigma_{pp}\left(\frac{E_{\pi^0}}{\kappa_\pi}\right) \frac{dn_{CR}}{dE}\left(\frac{E_{\pi^0}}{\kappa_\pi}\right) \tag{2.32}$$

In order to estimate the number of gamma rays of a certain energy produced by the decay of neutral pions π^0, one first can notice that, in the rest frame of the π^0, the gamma photons will have the half of the inertial energy of the parent pion,

$$E_{\gamma,\, RF} = \frac{1}{2} m_{\pi^0}\, c^2 \tag{2.33}$$

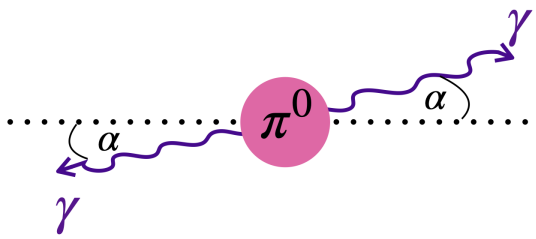

Figure 2.4 Representation of the decay of the neutral pion π^0 into two gamma-photons in the rest-frame of the π^0.

where m_{π^0} es the mass of the pion, and $E_{\gamma,\,RF}$ is the energy of one gamma-ray produced in the decay process, defined in the pion rest-frame (see figure 2.4). Then, given that before the proton-collisions the pions will commonly possess momentum, the energy E_γ of the emitted gamma-ray will depend on: (1) the angle α formed between the direction of motion of the parent π^0 and the direction of motion of the gamma-ray photon, and (2) the β parameter $(= v_{\pi^0}/c)$ of the produced pion. Thus, the energy of the gamma ray in the frame of the background gas E_γ, is given by

$$E_\gamma = E_{\gamma,\,RF}\frac{1}{\sqrt{1-\beta^2}}(1-\beta\,\cos\alpha) = \frac{1}{2}\frac{m_{\pi^0}\,c^2}{\sqrt{1-\beta^2}}(1-\beta\,\cos\alpha). \tag{2.34}$$

Considering an isotropic distribution of gamma rays in the pion rest-frame, such that α changes randomly from one pion rest-frame to other, one can first estimate the number of gamma-ray photons per unit energy taking the differential expression of Eq. 2.34 assuming that all neutral pions have the same Lorentz factor, such as

$$\frac{dN_\gamma}{dE_\gamma} = \frac{2\sqrt{1-\beta^2}}{\beta m_{\pi^0}\,c^2}\frac{dN_\gamma}{d\cos\alpha}. \tag{2.35}$$

Noting that relativistic momentum of the neutral pions is given by $pc = m_{\pi^0}v_{\pi^0}c/\sqrt{1-\beta^2} = \sqrt{E_{\pi^0}^2 - m_{\pi^0}^2c^4}$, and that the number of gamma-photons per solid-angle can be estimated as

$$\frac{dN_\gamma}{d\Omega} = \frac{dN_\gamma}{2\pi d\cos\alpha} \approx \frac{2N_{\pi^0}}{4\pi}, \tag{2.36}$$

the number of gamma-ray photons emitted per unit energy is given by

$$\frac{dN_\gamma}{dE_\gamma} = \frac{2N_{\pi^0}}{\sqrt{E_{\pi^0}^2 - m_{\pi^0}^2c^4}} \tag{2.37}$$

The equation 2.37 suggest a flat spectrum for the gamma-ray energy distribution from the decay of neutral pions with energies $= m_{\pi^0}c^2/\sqrt{1-\beta^2}$. In order to generalize this result, a certain number neutral pions N_{π^0} in a range of energy dE_{π^0} must be considered, so

$$d\Big(\frac{dN_\gamma}{dE_\gamma}\Big) = \frac{2}{\sqrt{E_{\pi^0}^2 - m_{\pi^0}^2c^4}}\frac{dN_{\pi^0}}{dE_{\pi^0}}dE_{\pi^0} \tag{2.38}$$

$$\Rightarrow \frac{dN_\gamma}{dE_\gamma} = \int dE_{\pi^0}\frac{2}{\sqrt{E_{\pi^0}^2 - m_{\pi^0}^2c^4}}\frac{dN_{\pi^0}}{dE_{\pi^0}}. \tag{2.39}$$

Then, the expression that represents the rate of gamma-ray photons produced per time and energy units for a pion decay process, is given by

$$\frac{dq_\gamma}{dE_\gamma}(E_\gamma) = \int_{E_\gamma}^{\infty} dE_{\pi^0}\ \frac{2}{\sqrt{E_{\pi^0}^2 - m_{\pi^0}^2c^4}}\frac{dq_{\pi^0}}{dE_{\pi^0}} \tag{2.40}$$

where $q_\gamma = dN_\gamma/dt$, and dq_{π^0}/dE_{π^0} is given by Eq. 2.32.

With this expression for the gamma-ray emission, one can estimate the gamma-ray flux, which corresponds to the number of gamma-ray photons per unit area, time and energy, that comes from the source to Earth. Assuming that R_E is the distance from the source to Earth, the gamma-ray flux Φ_γ that reaches the Earth's atmosphere is given by

$$\Phi_\gamma(E_\gamma) = \frac{1}{4\pi R_E^2}\int dV\frac{dq_\gamma}{dE_\gamma} = \frac{2c}{R_E^2}\int_{E_\gamma}^{\infty} dE_\pi \int dr\ r^2\ \frac{1}{\sqrt{E_\pi^2 - m_{\pi^0}^2c^4}}\frac{dq_{\pi^0}}{dE_{\pi^0}}, \tag{2.41}$$

where spherical symmetry has been assumed for the emission volume, and r is the radial variable of this volume. Then, from Eq. 2.32, one can estimate the gamma-ray flux per unit gamma-ray energy E_γ received at Earth as

$$\Phi_\gamma(E_\gamma) = \frac{2c}{R_E^2\kappa_\pi}\int_{E_{\min}}^{\infty} dE_{\pi^0}\frac{\sigma_{pp}(E)}{\sqrt{E_{\pi^0}^2 - (m_{\pi^0}c^2)^2}}\int_{r_{\min}}^{\infty} dr\ r^2 n_g(r)\frac{dn_{CR}}{dE}(E,r), \tag{2.42}$$

where $E_{\min} = E_\gamma + m_{\pi^0}^2c^4/4E_\gamma$, the energy of CRs E is such that $E = m_pc^2 + \frac{E_\pi^0}{\kappa_\pi}$, E_{π^0} is the energy of the neutral pion produced in the collisions, m_p and m_{π^0} are the proton and pion masses, $\kappa_\pi \approx 0.17$ is the mean fraction of the CR kinetic energy transferred to neutral pions in the collisions [26], $d \approx 8\,\mathrm{kpc}$ is the distance between Sgr A* and the Earth, $n_g(r)$ is the gas background density define in Eq. 2.1, and $r_{\min}$ is the minimum radius considered for the emissivity calculation. The cross-section for π^0 production through proton-proton collisions is given by [26]

$$\sigma_{pp}(E) \approx 4\times10^{-26}\,\mathrm{cm}^2\ \left(1 + 0.04\ \ln\frac{E - m_pc^2}{\mathrm{TeV}}\right). \tag{2.43}$$

Chapter 3

Results

3.1 CR density distribution

In cases where the transport of CRs is dominated by turbulent magnetic field effects, the transport of CRs will be mainly determined by diffusive processes. By reordering terms in Eq. 2.7, the CR density per energy units is describe as

$$\frac{dn_{CR}}{dE}(E,r) = -\frac{dN}{dEdt}(E) \int dr' \, \frac{D(E,r')^{-1}}{4\pi r'^2}. \tag{3.1}$$

Substituting the expression for the diffusion coefficient in the low-energy diffusive (LED) regime and high-energy diffusive (HED) regime (Eqs. 2.26 and 2.26, respectively) in Eq. 3.1, and considering the number of injected CRs per energy and time, $dN(E)/dEdt$, given by Eq. 2.4, one obtains that:

- If $R_L \ll l_c$, the CR density is modeled as

$$\begin{aligned}\frac{dn_{CR}}{dE}(E,r) = 3.0\,\mathrm{erg}^{-1}\mathrm{cm}^{-3}\,\frac{f(q,E_{max})}{1+\frac{1}{3}(n+2m)} \\ \left(\frac{E}{1\mathrm{TeV}}\right)^{-(1/3+q)} \left(\frac{r}{10R_g}\right)^{-(1+\frac{1}{3}(n+2m))} \hat{Q}\,(\hat{l}_c\,21000^{-m})^{-2/3}\,\hat{B}^{1/3} + C,\end{aligned} \tag{3.2}$$

  where C is a constant of integration characterized by the different continuity and boundary conditions (see Fig. 3.1).

- If $R_L \gg l_c$, the CR density is modeled as

$$\begin{aligned}\frac{dn_{CR}}{dE}(E,r) = 10^9\,\mathrm{erg}^{-1}\mathrm{cm}^{-3}\,\frac{f(q,E_{max})}{1+2n-m} \\ \left(\frac{E}{1\mathrm{TeV}}\right)^{-(2+q)} \left(\frac{r}{10R_g}\right)^{-(1+2n-m)} \hat{Q}\,\hat{l}_c\,21000^{-m}\,\hat{B}^2 + C.\end{aligned} \tag{3.3}$$

Cases where the transport of CRs is dominated by the background gas dynamic, the CR transport will be mainly determine by advection process. In this case the expression for the CR density distribution is obtained from Eq. 2.8, such that

$$\frac{dn_{CR}}{dE}(E,r) = \frac{v_{ad}(r)^{-1}}{4\pi r^2}\frac{dN(E)}{dEdt} \tag{3.4}$$

where we have simply assumed that the advection velocity corresponds to the velocity of the gas $v_{gas}(r)$, characterized by Eq. 2.29. Thus, the CR density distribution in the advection dominated (AD) regime is given by

$$\frac{dn_{CR}}{dE}(E,r) = \begin{cases} 3\times10^6\ \mathrm{cm^{-3}erg^{-1}}\hat{Q}f(q,E_{max})\left(\frac{E}{1\mathrm{TeV}}\right)^{-q}\left(\frac{r}{10R_g}\right)^{-3} & \text{if } 0.07\,\mathrm{pc} < r < 0.4\,\mathrm{pc} \\ 21\ \mathrm{cm^{-3}erg^{-1}}\hat{Q}f(q,E_{max})\left(\frac{E}{1\mathrm{TeV}}\right)^{-q}\left(\frac{r}{10R_g}\right)^{-2} & \text{if } r \geq\ 0.4\,\mathrm{pc}, \end{cases} \tag{3.5}$$

In order to determine the full expression for the CR density, continuity conditions must be imposed for two transitions in the transport of CRs. The first transition occurs when high-energy CRs diffusing out from the central source undergo a transition from the LED regime to HED regime at an energy-dependent radius r_C determined by the condition $R_L(E,r) = 0.38\,l_c(r)$, yielding

$$r_C(E) = \ 3\times10^{-6}\ \mathrm{pc}\left[\frac{1.3\times10^5\hat{l}_c\hat{B}}{(2.1\times10^4)^m}\right]^{1/(n-m)}\ \left(\frac{E}{\mathrm{TeV}}\right)^{-1/(n-m)}. \tag{3.6}$$

The second transition occurs for radii $r \gtrsim 0.07$ pc, i.e., in regions III and IV of the accretion flow defined in Chapter 2. This condition is achieve at certain radii $r_{C,ad}(E)$ from Sgr A*, at which

$$v_{diff}(E, r_{C,ad}(E)) = v_{gas}(E, r_{C,ad}(E)). \tag{3.7}$$

At lower energies, CRs transit from the LED regime to advection-dominated (AD) regime at a fixed radius $r = 0.07\,\mathrm{pc}$ because at these energies $v_{diff} < v_{gas}$. The energy separating these two cases, E_C, is determined by $r_C(E_C) = 0.07\,\mathrm{pc}$, which yields

$$E_C = \frac{1.3\times10^5\,(4.3\times10^{-5})^{n-m}}{(2.1\times10^4)^m}\,\hat{l}_c\,\hat{B}\,\mathrm{TeV}. \tag{3.8}$$

We obtain that, for case 2 in Table 3.1, this critical CR energy $E_C \approx 20\,\mathrm{TeV}$, in correspondence with that it is shown in Figure 3.2.

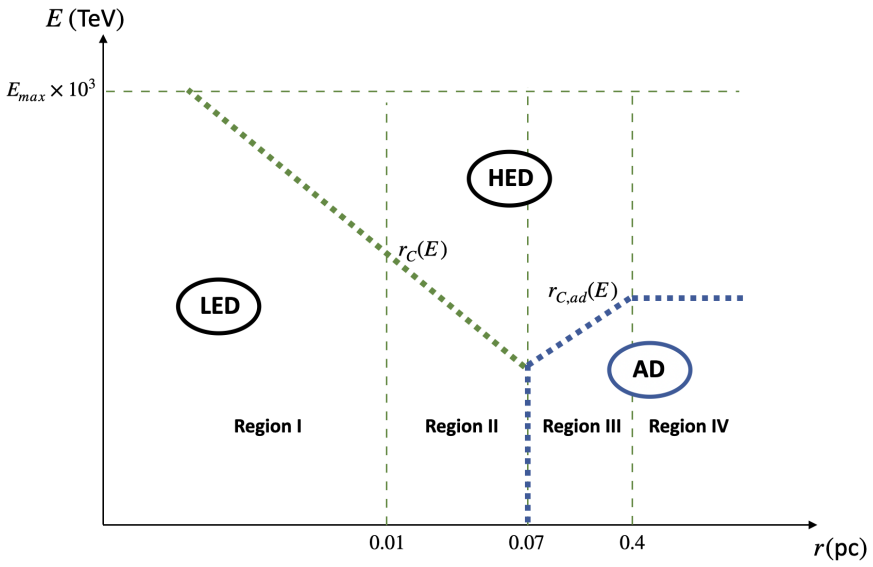

Figure 3.1 Boundary conditions for CR density. The dashed vertical lines separates the four region of the Sgr A* accretion flow described in Section 2.1

In figure 3.1 the transitions have been represented by segmented lines, green for the transition in the diffusion regimes and blue for the transition from diffusive to the advective regime. Thus, in order to ensure continuity in the CR density, we have imposed that

$$\frac{dn_{CR}}{dE}(E, r_C(E))|_{LED} = \frac{dn_{CR}}{dE}(E, r_C(E))|_{HED} \tag{3.9}$$

where the CR density in LED and HED regime are defined in Eq. 3.2 and 3.3, respectively, and the critical radius $r_C(E)$ is define in Eq. 3.6. For the LED to AD regime transition we have imposed that

$$\frac{dn_{CR}}{dE}(E, r = 0.07\text{pc})|_{LED} = \frac{dn_{CR}}{dE}(E, r = 0.07\text{pc})|_{AD}, \tag{3.10}$$

and for the HED to AD transition we consider that

$$\frac{dn_{CR}}{dE}(E, r_{C,ad}(E))|_{HED} = \frac{dn_{CR}}{dE}(E, r_{C,ad}(E))|_{AD} \tag{3.11}$$

These conditions will provide additional terms in the CR densities, which can be derived from the integration constants of Eqs. 3.2 and 3.3. For radii $r \gtrsim 0.4$ pc, it will be assumed that if $v_{diff} > v_{gas}$, only diffusion phenomena will be considered. For boundary conditions, it will be assumed that the CR density at sufficiently large distances is zero, that is $dn_{CR}(E, r \to \infty)/dE \to 0$.

Table 3.1. Different model parameter combinations.

	n	m	$\hat{Q}$	$\hat{l}_c$	$\hat{B}$	q	$E_{\rm max}$/PeV
Case 1	1	0	7.4	1.0	1	1.97	3
Case 2	1	0	12.6	3.0	1	1.97	3
Case 3	1	0	20.2	10.0	1	1.97	3
Case 4	0.9	0	6.2	1.0	1	1.97	3
Case 5	0.9	0	10.4	3.0	1	1.97	3
Case 6	0.9	0	18.3	10.0	1	1.97	3
Case 7	1	0.2	10.0	3.0	1	1.97	3
Case 8	1	0.4	9.0	3.0	1	1.97	3
Case 9	0.9	0.2	5.4	1.2	1	1.97	3
Case 10	0.9	0.4	4.3	1.2	1	1.97	3

According to the above modeling, we can now estimate the CR density dn_{CR}/dE in the Sgr A* accretion flow, for a given set of values of our model parameters: q, $\hat{Q}$, $E_{\rm max}$, $\hat{B}$, $\hat{l}_c$, n, and m. Figure 3.2 shows an examples of the CR density profile for a given combination of parameters (Cases 2 in Table 3.1), where we can identify three main regions:

I) **LED regime**: This regime is shown by the maroon region in Fig. 3.2. In this region, CR transport is dominated by diffusion, with $\lambda_{\rm mfp}$ in the $R_L < 0.38\, l_c$ regime of Eq. 2.25. The CR density is describe by Eq. 3.2, where the boundary and continuity term (associated to the integration constant) are subdominant.

II) **HED regime**: In this case, CR transport is also dominated by diffusion, but with $\lambda_{\rm mfp}$ in the $R_L > 0.38\, l_c$ regime of Eq. 2.25. In this case, the CR density, is described by Eq. 3.3, dropping off much faster with increasing r, as seen in the upper right corner of Fig. 3.2. Similarly to the LED regime, the terms that ensure continuity of dn_{CR}/dE, are also subdominant.

III) **AD regime**. In this regime, CR propagation is dominated by advection, and their density is given by

$$\frac{dn_{CR}}{dE}(E,r) = \, 3\times 10^6\,{\rm cm}^{-3}{\rm erg}^{-1}\hat{Q}\, f(q,E_{\rm max})\left(\frac{E}{1{\rm TeV}}\right)^{-q}\left(\frac{r}{10R_g}\right)^{-3} \tag{3.12}$$

for 0.07 pc $\leq r \leq$ 0.4 pc, and

$$\frac{dn_{CR}}{dE}(E,r) = \, 21\,{\rm cm}^{-3}{\rm erg}^{-1}\hat{Q}\, f(q,E_{\rm max})\left(\frac{E}{1{\rm TeV}}\right)^{-q}\left(\frac{r}{10R_g}\right)^{-2} \tag{3.13}$$

for $r >$ 0.4 pc, where again in both cases the CR density drops off much faster with increasing r than in the LED regime, as seen in the lower right corner of Fig. 3.2.

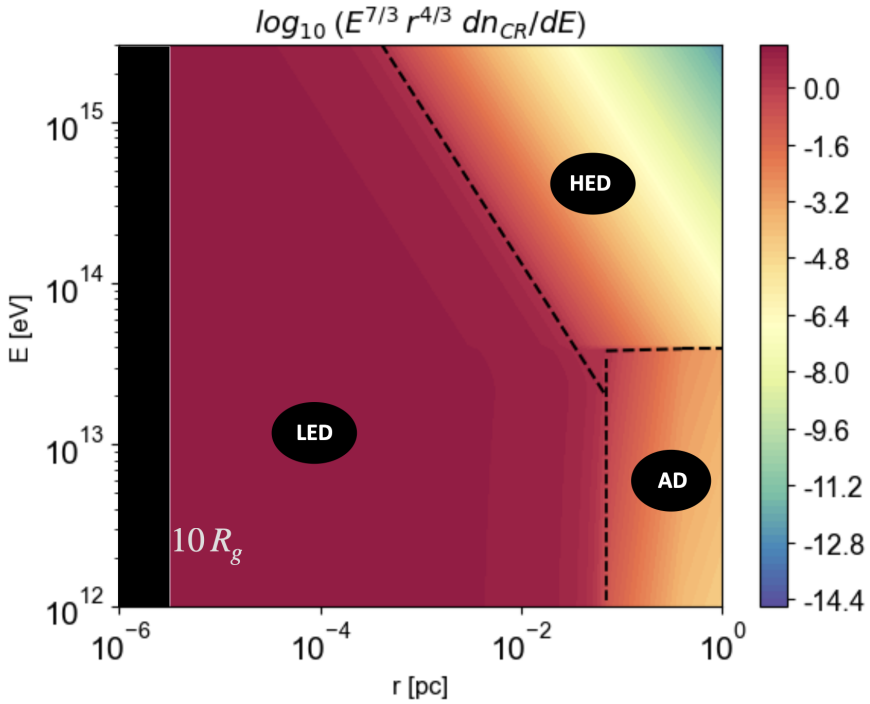

Figure 3.2 CR density per unit energy as a function of the radial coordinate r (horizontal axis) and the CR energy E (vertical axis) for Case 2 in Table 3.1. The color scale is normalized in units $\log_{10}(\mathrm{erg}^{-2/3+q}\,\mathrm{cm}^{-2+1/3(n+2m)})$, and the dashed lines mark the boundaries of the three CR transport regimes discussed in the text, namely low-energy diffusion (LED), high-energy diffusion (HED), and advection-dominated (AD).

3.2 Gamma-ray emission spectrum

For the estimation of the gamma-ray flux we use the expression for the hadronic emission obtained in section 2.4 incorporating the results obtained in the previous section for the CR density, $dn_{CR}/dE(E,r)$, and considering the proton-proton cross section given by Eq. 2.43 in all the estimations, including the 'LED model´ presented in Fig. 3.3 (blue dashed line) and the gamma-ray flux per unit $\log(r)$ presented in Fig. 3.4. The simplified model shows in Fig. 3.3 (green dashed line) was estimated considering the energy-independent part of cross-section Eq. 2.43.

As a result of the different behaviors of the CR diffusion above and below the critical energy $E_C(r)$ (result of reordering terms in Eq. 3.6), our model produces gamma-ray spectra consisting of two approximate power-laws joined at a break energy $E_{\gamma,b} = \kappa_\pi E_C(r = 0.07\,\mathrm{pc})$, similar to that observed in the spectrum of HESS J1745-290 source [6]. One example of this is shown in Figure 3.3, corresponding to Case 2 in Table 3.1. Interestingly, one can see in the maroon part of Fig. 3.2, the CR density is dominated in the LED regime. Based on this, it is expected that the gamma ray flux to be influenced by this dominant effect on the density of CRs. In fact, Fig. 3.4 shows that the gamma-ray flux coming principally from the LED regime, with a maximum near the diffusion transition. Thus, for $E_\gamma \lesssim E_{\gamma,b}$, the gamma ray spectrum is expected to have a low-energy spectral index with approximately the same value as the spectral index of the CRs in the LED region ($q+1/3 \approx 7/3$, as shown in Fig 3.2), while

the high-energy spectral index for $E_\gamma \gtrsim E_{\gamma,b}$, should be steeper given the energy-dependent depletion of CRs of $E > E_C$ at $r > r_C(E) \propto E^{-1/(n-m)}$.

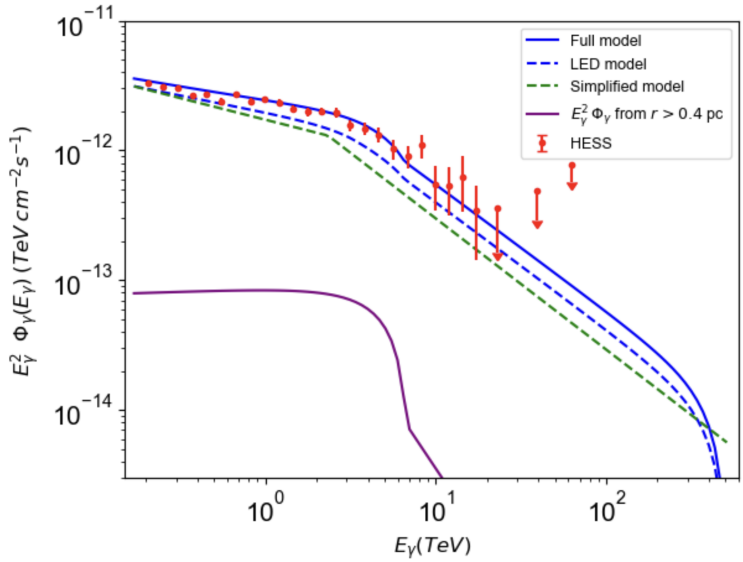

Figure 3.3 Models for the gamma-ray spectrum of HESS J1745−290 with the parameters of case *2* of Table 1. The solid blue line represents the total gamma-ray emission calculated from the full model. The dashed blue line is the "LED model", considering only the emission from CRs in the LED regime. The dashed green line shows our simplified model, given by Eqs. (3.14) and (3.15). The solid purple line represents the contribution from CRs at $r > 0.4$ pc. The red dots correspond to the H.E.S.S. measurements [2].

The fact that the gamma-ray spectrum is essentially determined by the shape of the LED region in Fig. 3.2, can also be inferred by calculating $\Phi(E_\gamma)$ assuming that gamma-ray emission is only produced by CRs in the LED regime (i.e., assuming $dn_{CR}/dE = 0$ in the HED and AD regimes). This calculation is shown by the blue dashed line in Fig. 3.3, which shows a similar broken power-law behavior as in the full calculation (blue solid line). Thus, the predicted emission in our model is essentially determined by the CRs in the LED regime, and its broken power-law behavior is a consequence of the energy-dependent transition in the CR diffusion regime at $r_C(E)$ for $E > E_C$.

3.3 Previous constraints on parameters

Since our purpose is to build a gamma-ray emission model compatible with the observed spectrum of HESS J1745-290, we need to find the set of model parameters that achieve that goal. Our model parameters are essentially seven: q, $\hat{Q}$, E_{max}, n, $\hat{B}$, $\hat{l}_c$ and m. The first three parameters are related to the characteristics of the CRs injected by Sgr A*, while the last four are related to the assumed properties of the magnetic turbulence where the CRs propagate. In order to find the parameters that are most suitable to reproducing HESS J1745-290, in this section we discuss the previously known constraints on these parameters. The injection parameters q, $\hat{Q}$ and $E_{\rm max}$ have to obey restrictions from the diffuse emission

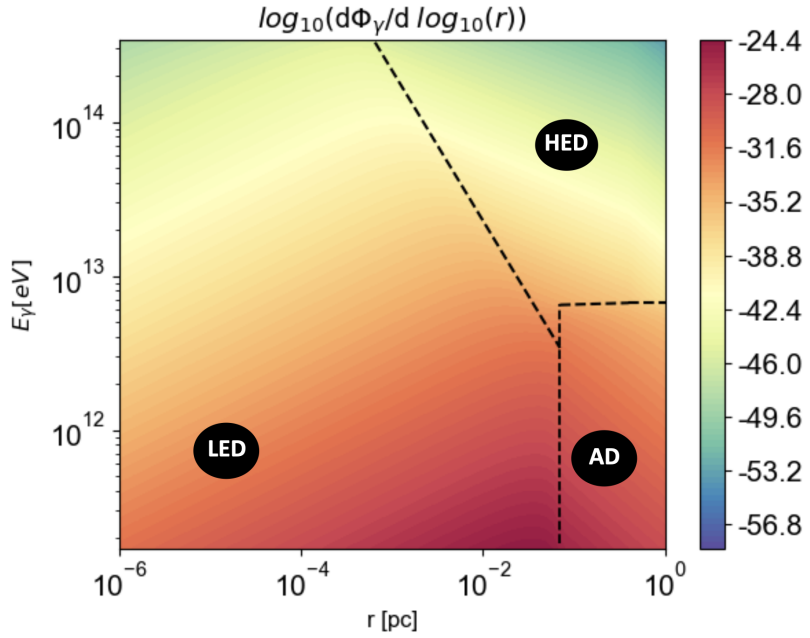

Figure 3.4 Gamma-ray flux per unit $\log(r)$. The differential emission was calculated for the Case 2 in Table 3.1

in the CMZ. This emission has been found to be consistent with a CR proton spectral index of $\Gamma_p \approx 2.3$ [2]. This, however, does not correspond to the index q of the injected CRs, since the CR spectrum in the CMZ is also affected by the energy-dependent residence time of the CRs in this region, which is inversely proportional to the CR diffusion coefficient in the CMZ, assumed to have a power-law shape, $D_{\rm CMZ}(E) \propto E^{\delta}$. This implies that $\Gamma_p = q + \delta$, with the value of δ likely between $\delta \approx 1/3$ and $1/2$, as expected for Kolmogorov and Kraichnan types of magnetic turbulence, respectively [5]. Thus, a reasonable expectation for q is $q \approx 1.9 - 2.1$. Also, making different assumptions regarding the magnitude of $D_{\rm CMZ}(E)$, Abramowski et al. 2016 [2] and Scherer et al. 2022 [52] found the CR injection power for $E > 10$ TeV to be $Q(E > 10\,{\rm TeV}) \approx 8 \times 10^{37} {\rm erg\,s^{-1}}$ and $Q(E > 10\,{\rm TeV}) \approx 3 \times 10^{36} {\rm erg\,s^{-1}}$, respectively. This implies $\hat{Q} \approx 13$ and 2, respectively. Additionally, the diffuse emission restricts the maximum CR energy to $E_{\rm max} \gtrsim 1$ PeV [2, 4].

The restrictions to the parameters n and $\hat{B}$ can be obtained from previous MHD simulations of the Sgr A* accretion flow. For instance, [49] shows that assuming a beta parameter in the winds of the Wolf-Rayet stars $\beta_W = 10^4$ (which correspond to the rate between the magnetic and wind pressure), the magnetic field near Sgr A* reaches the value $B(r = 10R_g) \approx 10$ G ($\hat{B} \approx 1$), and the parameter n (defined in Eq. 2.2) is approximately $n \approx 1$. In the case of $\beta_W = 10^2$ they obtain essentially the same $\hat{B} \approx 1$, while $B(r = 0.1\,{\rm pc})$ is a factor ~ 4 larger than in the $\beta_W = 10^4$ case. For our assumed power-law dependence $B \propto r^{-n}$ (Eq.2.2), this implies $n \approx 0.9$.

Given these considerations, we will restrict our analysis to cases with $\hat{B} = 1$ and, in order to be consistent with the spectral index suggest in Abramowski et al. [2] ≈ 2.3, we also restrict $q = 2.3 - 1/3 \approx 2$ (see Eq. 3.16), and will consider two possible values for n, $n = 1$ and 0.9. We will show that with these choices of parameters our model can reproduce

the main features of the emission from HESS J1745-290 quite well, respecting the other restrictions from the diffuse CMZ emission: $\hat{Q} \approx 2-13$ and $E_{\rm max} \gtrsim 1$ PeV. Regarding the more uncertain parameters $\hat{l}_c$ and m, we will show that, fitting the data of HESS J1745-290 is strongly dependent on $\hat{l}_c$ being in the range $\hat{l}_c \approx 1-3$ (for $n = 1$ and 0.9, respectively), while having a weaker dependence on m.

3.4 Simplified model

We showed that the main features of the emission from our model can be reproduced by considering only particles in the LED regime. One can thus build a simple analytical emission model recalculating the emission produced by the CRs in the LED regime, but ignoring the (weak) energy-dependence of σ_{pp} (by fixing $E = 1$ TeV in Eq. 2.43). This way, we obtain relatively simple expressions for $\Phi_\gamma(E_\gamma)$, which preserve the main features of our model (as shown by the dashed-green line in Fig. 3.3), while showing the effect of the model parameters on the emitted spectrum. For $E_\gamma \lesssim E_{\gamma,b}$,

$$\begin{aligned}\Phi_\gamma(E_\gamma) \approx & 1.3\times10^{-9}(2.1\times10^4)^{-\frac{n}{3}}\,\frac{f(q,E_{\rm max})\,\hat{Q}\,\hat{l}_c^{-\frac{2}{3}}\,\hat{B}^{\frac{1}{3}}}{1-\frac{1}{9}(n+2m)^2} \\ & \times\,\frac{\kappa_\pi^{q-\frac{2}{3}}}{q+\frac{1}{3}}\left(\frac{E_\gamma}{\rm TeV}\right)^{-q-\frac{1}{3}}\ {\rm TeV}^{-1}\,{\rm cm}^{-2}\,{\rm s}^{-1},\end{aligned} \tag{3.14}$$

while, for $E_\gamma \gtrsim E_{\gamma,b}$,

$$\begin{aligned}\Phi_\gamma(E_\gamma) \approx & 1.5\times10^{-10}\,6.2^{-\frac{m}{n-m}}\,(2.1\times10^4)^{-\frac{m(2-n)}{n-m}}\,\frac{f(q,E_{\rm max})\,\hat{Q}}{1-\frac{1}{9}(n+2m)^2} \\ & \times\,\frac{\kappa_\pi^{q+\frac{1-n}{n-m}}}{q+\frac{1-m}{n-m}}\,\hat{l}_c^{\frac{1-n}{n-m}}\,\hat{B}^{\frac{1-m}{n-m}}\left(\frac{E_\gamma}{\rm TeV}\right)^{-q-\frac{1-m}{n-m}}\ {\rm TeV}^{-1}\,{\rm cm}^{-2}\,{\rm s}^{-1},\end{aligned} \tag{3.15}$$

both of which are represented by the dashed green line in Fig. 3.3.

In order to reproduce the observations of HESS J1745-290, the broken power-law predicted by our model needs to reproduce the values for its low and high-energy indices, α_{LE} and α_{HE}, and the energy of the spectral break $E_{\gamma,b}$.

Low and high-energy indices: Eq. 3.14 predicts

$$\alpha_{LE} = q + \frac{1}{3}, \tag{3.16}$$

while Eq. 3.15 predicts

$$\alpha_{HE} = q + \frac{1-m}{n-m}. \tag{3.17}$$

As was mentioned, assuming $q \approx 2$, our model predicts $\alpha_{LE} \approx 2.3$, which agrees well with the observed α_{LE} [2], as can be seen from Figure 3.3. Also, at high energies, our model

predicts $\alpha_{HE} \approx q + (1-m)/(n-m) \approx 3$, in good agreement with the observations [2]. Given the range of values assumed for n and m, we expect α_{HE} to be close to 3 and fairly independent of the value of m. Interestingly, the slope $\alpha_{HE} \approx 3$ obtained in our Case 2 (with $n = 1$) at high energies ($E_\gamma \gtrsim 3$ TeV) appears to be consistent with the H.E.S.S. data (as seen in Fig. 3.3), although a somewhat softer spectrum (smaller α_{HE}) may work similarly well. Thus, $q \approx 2$ produces a broken power-law in the gamma-ray emission whose indices correspond reasonably well to those of the observed HESS J1745-290 spectrum, while being consistent with the injection spectral index required to explain the diffuse emission in the CMZ.

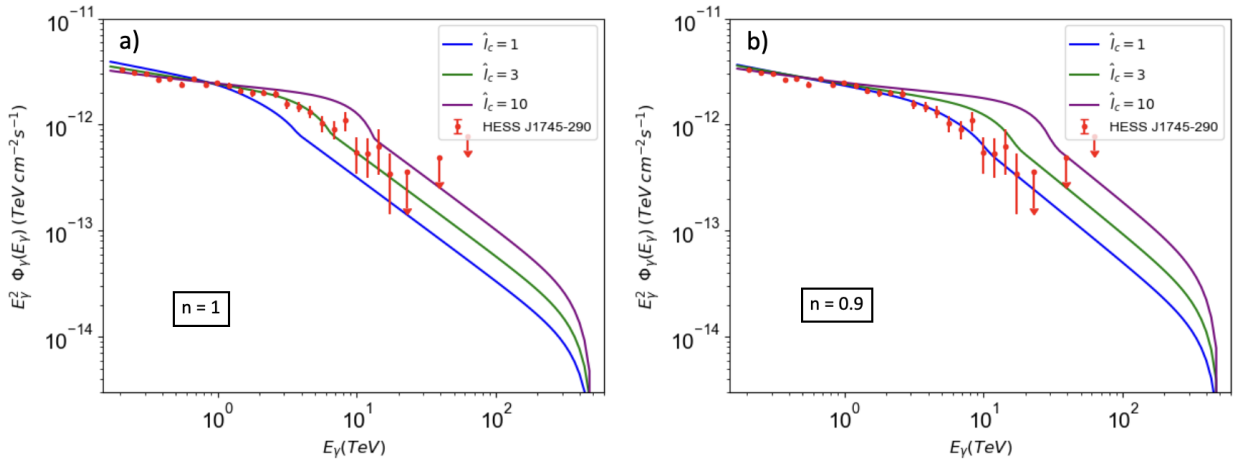

Figure 3.5 Spectral energy distribution of the gamma-ray flux for different coherence length and magnetic field profiles. The upper panel shows the estimated gamma-ray emission for different coherence lengths, assuming $B \sim r^{-1}$. The bottom panel shows the estimated gamma-ray emission for different coherence lengths, assuming $B \sim r^{-0.9}$ (see Table 3.1).

Spectral break energy: If $E_{\gamma,b} \approx 3$ TeV, the critical energy $E_C \approx E_{\gamma,b}/k_\pi \approx 20$ TeV. Considering Eq. (3.8), and noting that in this equation the terms with m indices can be approximately simplified, one can show that

$$E_C \approx 6\ \text{TeV}\ (2.1 \times 10^4)^{1-n} \hat{l}_c \hat{B}. \tag{3.18}$$

Since $\hat{B} \approx 1$ and $n \approx 0.9 - 1$, this strongly constrains $\hat{l}_c \approx 1 - 3$.

3.5 Constraints from our full model

We use our full model to show the way our parameters are restricted by the main features of the HESS J1745-290 spectrum. The restrictions on l_c can be seen from Figure 3.5, which shows the calculated gamma-ray spectrum for cases with $l_c = 1$, 3 and 10 and the same parameters $n = 1$, $m = 0$, $\hat{B} = 1$, $q = 1.97$ and $E_{\max} = 3$ PeV (Cases 1, 2 and 3 in Table 3.1). The only other different parameter between these cases is $\hat{Q}$, which is adjusted so that they all have the same flux at E_γ =1 TeV, to ease comparison. We see in Figure 3.5*a* that the case

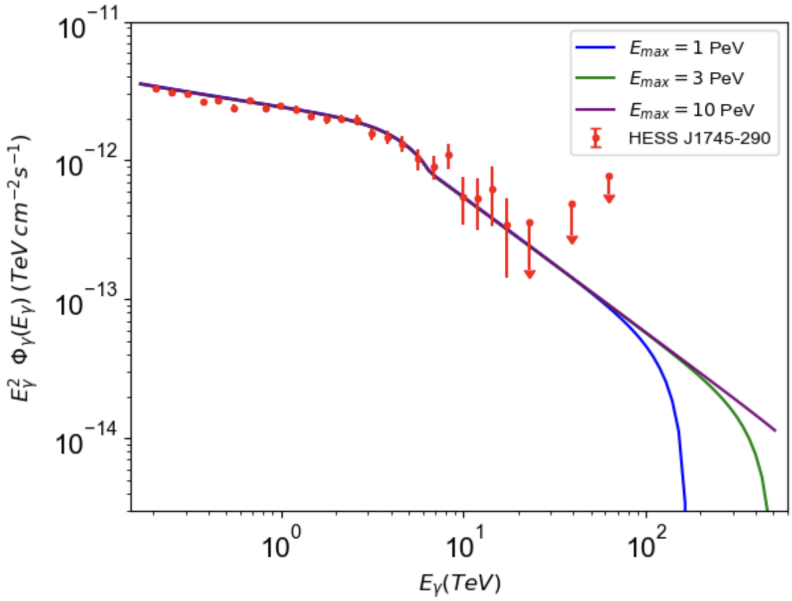

Figure 3.6 Spectral energy distribution of the gamma-ray emission for different maximum energies $E_{\rm max}$ considered in the CR injection. The values for m, n, $\hat{l}_c$ and $\hat{B}$ correspond to those of *case 2* in Table 3.1.

$\hat{l}_c = 3$ is favored by the HESS J1745-290 data and that, as expected, the effect of increasing l_c while keeping the same n and $\hat{B}$ is to proportionally increase E_C and, therefore, the energy of the spectral break $E_{\gamma,b}$ in the emission spectrum (as shown by Eq. 3.18). Figure 3.5*b* shows the same calculations but assuming $n = 0.9$ instead of $n = 1$ (cases 4, 5 and 6 in Table 3.1). We see a similar behavior as in Fig. 3.5*a*, except that the three spectral breaks occur at gamma-ray energies ~ 3 times larger, consistent with the factor $(2100)^{1-n} \approx 3$ in Eq. 3.18. In this case, $\hat{l}_c = 1$ is favored by the HESS J1745-290 data. Equation 3.18 shows that cases with different $\hat{l}_c$ can, or course, produce the same $E_{\gamma,b} \approx 3$ TeV as long as $\hat{B}$ and n are adjusted accordingly. However, the fact that MHD simulations favor $\hat{B} \sim 1$ strongly support that $\hat{l}_c \approx 1-3$ for $n = 0.9-1$. The condition $\hat{l}_c \approx 1-3$ constitutes a strong constraint from our model on the characteristics of the MHD turbulence in Sgr A* accretion flow.

Figs. 3.5*a* and 3.5*b* also show a cutoff in the flux at $E_\gamma \sim 500$ TeV for all the cases shown (cases 1-6 in Table 3.1). This is consistent with the fact that gamma-rays of energy $E_\gamma \gtrsim 500$ TeV should be produced by CRs with $E \gtrsim 500/\kappa_\pi$ TeV ≈ 3 PeV, which are not present for $E_{\rm max}$=3 PeV, as assumed in cases 1-6. This effect of $E_{\rm max}$ on the cutoff energy of the gamma-rays can also be seen from Fig. 3.6, which shows the spectrum for cases with $E_{\rm max} = 1$, 3 and 10 (cases 7, 2 and 10, respectively), which have the same values for the parameters n, m, q, $\hat{B}$, $\hat{l}_c$, and slightly different $\hat{Q}$ so that the three spectra visually fit the HESS J1745-290 data.

Regarding the role of m, in section 3.4 we used approximate expressions for $\Phi_\gamma(E_\gamma)$ to show that the parameter m does not affect significantly the spectral index of the gamma-ray spectrum at low or high energies (α_{LE} and α_{HE}, respectively) nor the gamma-ray energy that separates these two power-law regimes ($E_\gamma \sim 6$ TeV). This is fairly confirmed by Fig. 3.7*a*, which shows the emission calculations for cases with $n = 1$ and $m = 0, 0.2$ and 0.4

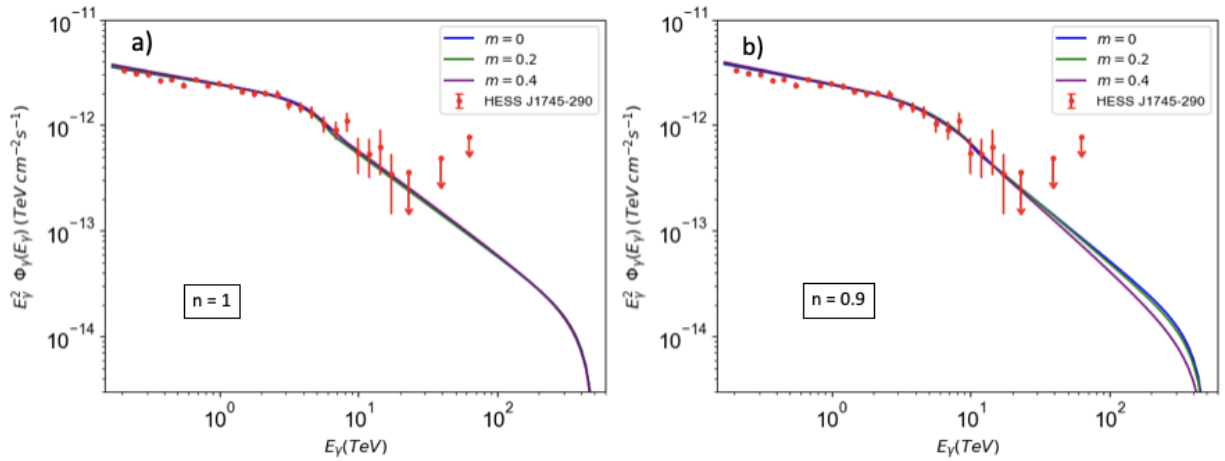

Figure 3.7 Spectral energy distribution of the gamma-ray emission considering different magnetic fields and magnetic turbulence profiles. The model parameter combinations are specified in Table 3.1.

(cases 2, 7 and 8 in Table 3.1; all the other parameters are the same).

Notice that Fig. 3.7 shows that for $n = 1$, m does not modify the slope of the high energy part of the gamma-ray spectrum α_{HE}. This is consistent with Eq. 3.17, which predicts no dependence of α_{HE} on m for $n = 1$. However, this equation implies that,in the case $n = 0.9$, increasing the parameter m can weakly decrease the index α_{HE} of the high energy emission, making this part of the spectrum steeper. This is indeed what is seen in Fig. 3.7*b*, which shows the emission spectra for cases with $n = 0.9$ and $m = 0, 0.2$, and 0.4 (cases 4, 9 and 10 in Table 3.1; the other parameters are the same).

We have thus shown that models with $\hat{B} = 1$ and $q \approx 2$, and $n = 1$ and 0.9 can reproduce well the main features of the emission from HESS J1745-290, including its break at $E_{\gamma,b} \approx 3$ TeV, respecting the restriction from diffuse CMZ emission: $E_{\rm max} \gtrsim 1$ PeV. This, however, establishes a strong restriction on $\hat{l}_c$, which needs to be in the range $\hat{l}_c \approx 1 - 3$ (for $n = 1$ and 0.9, respectively). Regarding m, its effect on HESS J1745-290 is rather weak and it only appears at $E_\gamma \gtrsim E_{\gamma,b}$. Remarkably, in the cases in which our model is capable to produce the best fits to HESS J1745-290 (Case 2 and Case 4 in Table 3.1 for $n = 1$ and $n = 0.9$, respectively) we find respectively $\hat{Q} \approx 7 - 13$, which is in good agreement with the estimate of Abramowski et al. 2016 and Scherer et al. 2022 [2, 52] .

Chapter 4

Consistency of assumptions

In this chapter we check the consistency of several simplifying assumptions made in the calculation of gamma-ray emission.

4.1 CR transport for radii $r > 0.4$ pc

Even though CR transport at radii $r > 0.4$ pc is expected to be a combination of advection and diffusion, in our calculations we have neglected the contribution from diffusion at those large radii. This leads to an overestimate of the CR density in this region and, therefore, provides an upper limit to its corresponding emission. In Fig. 3.3 we show in the purple line this upper limit to the gamma-ray emission from $r > 0.4$ pc. We see that it is less than $\sim 3\%$ of the total emission for all the energies of interest, so this overestimate should not affect the accuracy of our results.

Table 4.1. Different model parameter combinations for different minimum radii $r_{\rm min}$. For each case we assume $E_{\rm max} = 3$ PeV.

	n	m	$\hat{Q}$	$\hat{l}_c$	$\hat{B}$	q	$r_{\rm min}$
Case 11	1.0	0.0	12.8	3.0	1.0	1.97	3×10^{14} cm
Case 12	1.0	0.4	9.0	3.0	1.0	1.97	$< 10^{12}$ cm
Case 13	0.9	0.0	6.6	1.2	1.0	1.97	1.2×10^{14} cm
Case 14	0.9	0.4	4.3	1.2	1.0	1.97	$< 10^{12}$ cm

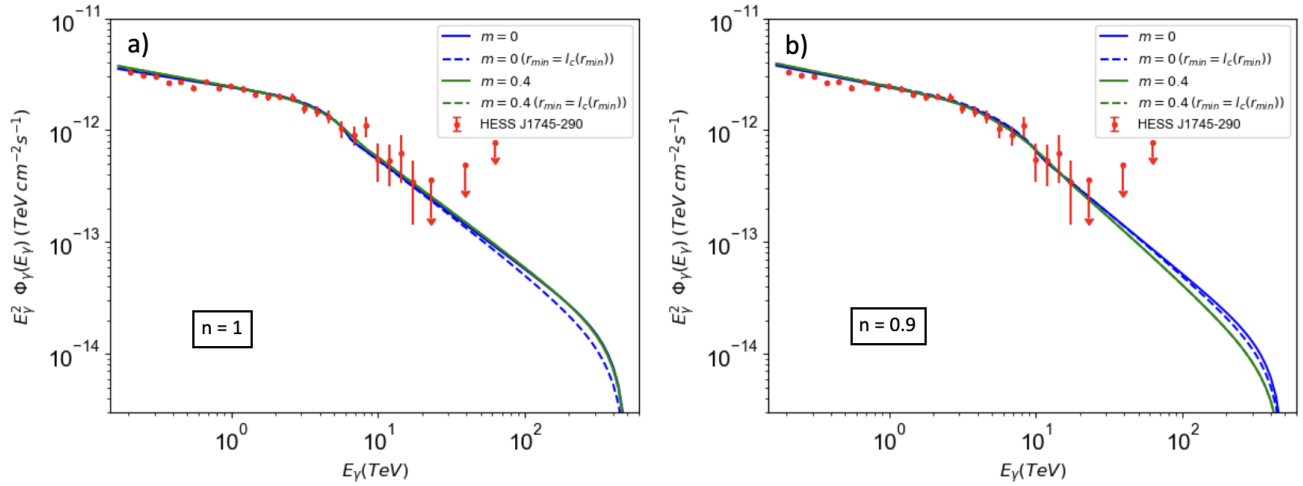

Figure 4.1 Spectral energy distribution of the gamma-ray emission for different minimum radii $r_{\rm min}$ of the emission region. The parameter combinations are specified in Table 4.

4.2 Minimum radius r for diffusion

In our emission calculations, we assumed that diffusion is the dominant process for CR transport at $r < 0.07$ pc. However, diffusive transport is a valid approximation for CR propagation only when $r \gg r_{\rm min}$, where $r_{\rm min}$ is defined by

$$r_{\rm min} = l_c(r_{\rm min}) \tag{4.1}$$

For $r \lesssim r_{\rm min}$, CR transport is presumably nearly ballistic along magnetic field lines. We note that, however, the existence of an approximately ballistic CR propagation at $r \lesssim r_{\rm min}$ should not affect the accuracy of our results. This is because the CR density at $r \lesssim r_{\rm min}$, for which diffusive transport was assumed, constitutes an upper limit to the density of ballistically propagating CRs and, at the same time, this overestimated CR density produces an emission negligible compared to the emission from all radii. The former point can be shown by noting that the propagation velocity of particles due to diffusion (obtained from Eqs. 2.26 and 2.9)

$$v_{\rm diff} \approx\ 2\times10^6\ 0.52^{2m}\ 14.4^{n-1}\ \hat{l}_c^{2/3}\ \hat{B}^{-1/3} \left(\frac{E}{\rm TeV}\right)^{1/3} \left(\frac{r}{0.01{\rm pc}}\right)^{\frac{1}{3}(n+2m)-1} {\rm cm/s}, \tag{4.2}$$

for all combinations of free parameters in our model, is always less than the speed of light. This means that our calculated CR density for $r \lesssim r_{\rm min}$ is larger or of the same order as the density obtained for a more realistic, nearly ballistic CR propagation.

The fact that our calculated emission from $r < r_{min}$ is negligible compared to the total emission from all radii can also be seen from Figure 4.1. This figure shows in dashed lines the same calculations as the solid lines, but removing the emission from $r < r_{min}$. We see that there is almost no difference between the dashed and solid lines, implying that the calculated emission from $r = 10^{12}$ cm to $r = r_{min}$ does not contribute significantly to the total emission.

4.3 Neglecting advection for $r < 0.07$ pc

Besides diffusion, advection can also contribute to CR transport due to the average radial gas velocity $v_{\rm gas}$ at $r < 0.07$ pc. As was mentioned in Section 2.1, according to the simulations of Ressler et al. [49], for $0.01\,{\rm pc} \lesssim r \lesssim 0.07\,{\rm pc}$ there is a stagnation region where the mass accretion rate averaged over the whole solid angle approaches $\dot{M} \approx 0$, indicating that $v_{\rm gas}$ should have a small effect on the CR transport in that region. In addition, for $r \lesssim 0.01$ pc there is an inflow dominated region where $\dot{M}$ is nearly constant. To neglect the effects of gas dynamics on the transport of CRs, the condition $v_{\rm gas} \ll v_{\rm diff}$ must be satisfied for the lowest energy CRs diffusing in the LED regime for all radii $r < 0.07$ pc (as seen in Fig. 3.2). Since we are focusing on emission with $E_\gamma \gtrsim 0.2$ TeV, the lowest CR energy needed to produce this emission is $E \gtrsim 0.2/\kappa_\pi$ TeV ≈ 1 TeV. The ratio $v_{\rm diff}/|v_{\rm gas}|$, given by

$$\frac{v_{\rm diff}}{|v_{\rm gas}|} \approx 20 \cdot 0.52^{2m}\, 14.4^{n-1} \hat{l}_c^{2/3} \hat{B}^{-1/3} \left(\frac{E}{\rm TeV}\right)^{1/3} \times \left(\frac{r}{0.01{\rm pc}}\right)^{\frac{1}{3}(n+2m)} {\rm cm/s}, \tag{4.3}$$

is an increasing function of r. Thus, neglecting advection requires $v_{\rm diff}/|v_{\rm gas}| > 1$ for $E = 1$ TeV and $r = r_{min}$, which, as we see above, is the lowest radius where the LED regime is valid. Fig. 4.2*a* shows $v_{\rm diff}/|v_{\rm gas}|$ for $E = 1$ TeV and at $r = r_{min}$, for the cases with $n = 1$ ($\hat{l}_c = 3$) and $n = 0.9$ ($\hat{l}_c = 1$), shown in blue and red, respectively, as a function of m. We see that for $n = 1$, neglecting advection requires $m \lesssim 0.2$, while for $n = 0.9$, neglecting advection requires $m \lesssim 0.1$. This result shows that the consistency of our calculations requires a fairly weak dependence of l_c on r, which is in correspondence with our assumptions.

Interestingly, the dependence on E of $v_{\rm diff}/|v_{\rm gas}|$ also implies that CRs of energies $E \ll 1$ TeV are significantly affected by advection, in principle not being able to propagate beyond $r \sim r_{\rm min}$. This implies that the gamma-ray emission for $E_\gamma \lesssim E_C \kappa_\pi$ is not captured by our model.

Advective transport of the CRs could also be produced by the random motions of the MHD turbulence in the accretion flow. We have also neglected this possibility for transport at $r < 0.07$ pc. If we estimate this turbulent velocity by the Alfvén velocity of the gas v_A and its length-scale by l_c, the motion of the turbulence eddies should induce a CR diffusion characterized by a turbulent diffusion coefficient D_t given by[27]

$$D_t \sim l_c v_A/3, \tag{4.4}$$

which allows us to estimate a turbulent diffusion velocity, v_{td} as

$$v_{td} = D_t/r. \tag{4.5}$$

Combining these relations, one can show that

$$\frac{v_{\rm diff}}{v_{td}} \approx 80\,(1.9)^m (4.3\times 10^4)^{n-1} \hat{l_c}^{-\frac{1}{3}} \hat{B}^{\frac{4}{3}} \Big(\frac{E}{\rm TeV}\Big)^{\frac{1}{3}} \Big(\frac{r}{0.01{\rm pc}}\Big)^{\frac{4}{3}(n-1)+\frac{5}{6}-\frac{m}{3}}. \tag{4.6}$$

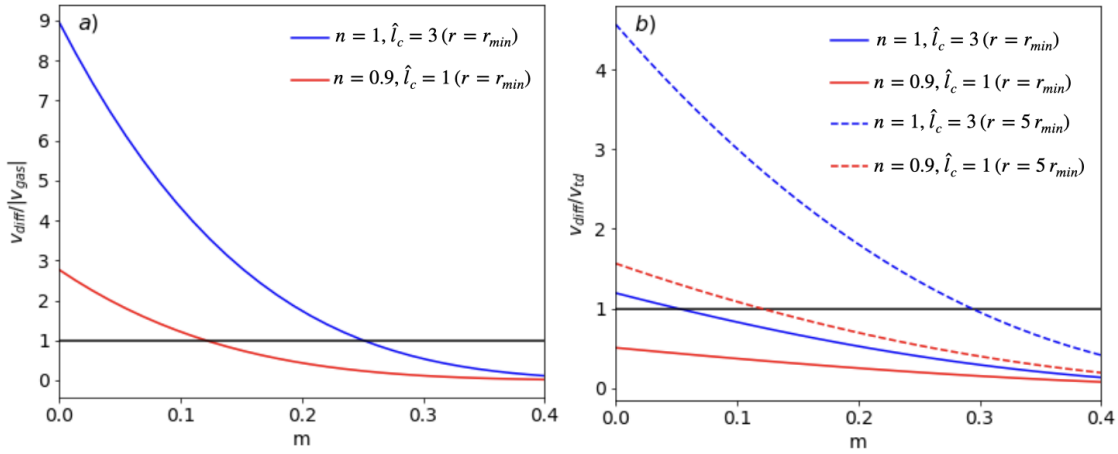

Figure 4.2 Comparison between the CR diffusion velocity and *(a)* the gas velocity (left panel), and *(b)* the turbulent diffusion velocity (right panel), for different radial profiles of the coherence length $l_c(r)$ and magnetic field $B(r)$. In the left panel the comparison was done considering a minimum radius r_{min} (given by eq. 4.1), whereas in the right panel the comparison was done for radii $r = r_{min} - 5\,r_{min}$.

However, similarly to what happens with diffusion and advection, the effect of turbulent diffusion should only be valid for $r \gtrsim r_{min}$. This means that, in order to neglect the effect of turbulent diffusion, we need $v_{\rm diff}/v_{td} \gtrsim 1$ for $E = 1$ TeV and $r = r_{min}$ (since $v_{\rm diff}/v_{td}$ is a growing function of r, as shown in Eq. 4.6). Panel *b* of Figure 4.2 shows $v_{\rm diff}/v_{td}$ for $E = 1$ TeV and at $r = r_{min}$, for the cases with $n = 1$ ($\hat{l}_c = 3$), and $n = 0.9$ ($\hat{l}_c = 1$), shown in blue and red, respectively, as a function of m. We see that only the case with $n = 1$ and $m \lesssim 0.05$ allows neglecting the effect of turbulent diffusion. However, if we evaluate Eq. 4.6 for $r = 5\,r_{min}$ (shown in dashed lines), $v_{\rm diff}/v_{td}$ becomes larger than unity essentially for the same cases in which $v_{\rm diff}/v_{\rm gas} > 1$. This means that turbulent diffusion may play a role in the outward transport of CRs only in the restricted radial range $r \sim r_{\rm min} - 5\,r_{\rm min}$, where the contributions of $v_{\rm diff}$ and v_{td} to CR transport are comparable. Therefore, we have neglected the contribution from turbulent diffusion in our calculations.

4.4 CR pressure and gas pressure

Our calculations assume that the gas properties in the accretion flow are determined by the hydrodynamic evolution of the wind of ~ 30 Wolf-Rayet stars that feed Sgr A*, as in the simulations of Ressler et al. 2018, 2020 [49, 48] on which our results are based. However, the presence of CRs diffusing out from the central black hole can be dynamically important in this evolution if the CR pressure becomes comparable to the gas pressure. Figure 4.3 shows these two pressures as a function of r for the cases 2 and 4 in Table 3.1. The CR pressure is calculated as

$$P_{CR}(r) = \frac{1}{3}\int_{E_{min}}^{E_{\rm max}} dE\; E\; \frac{dn_{CR}(E,r)}{dE}, \tag{4.7}$$

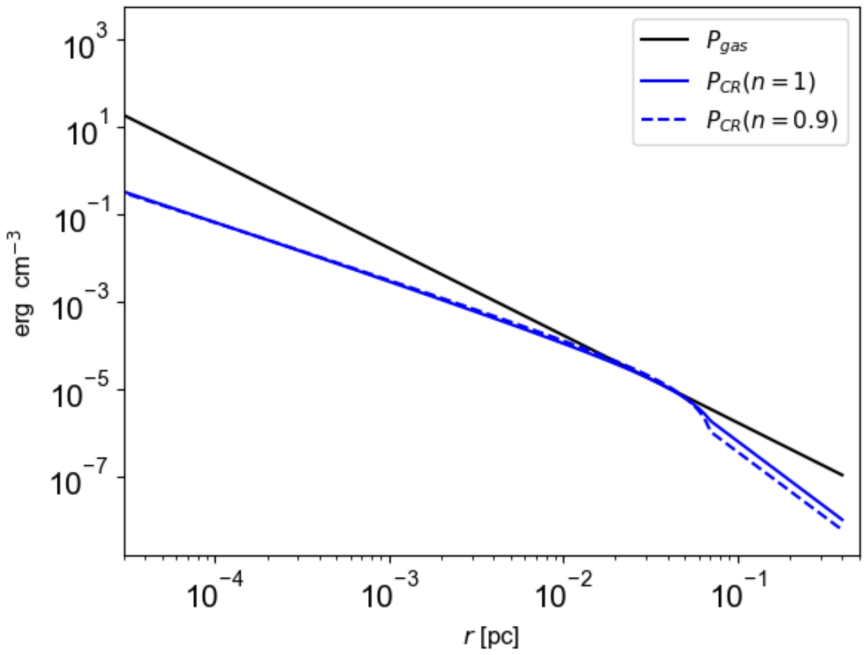

Figure 4.3 Cosmic-ray and gas pressure comparison. The values for the parameters used in the estimation of the CR pressure was done for Case 2 and Case 4 in Table 3.1

where $E_{min} = 1$ TeV, $E_{\max} = 3$ PeV, while the gas pressure is calculated as

$$P_{gas}(r) = 2\, k_B\, T(r) n_g(r), \tag{4.8}$$

where k_B is the Boltzmann constant, $n_g(r)$ is the gas density specified in Eq. 2.1, and $T(r)$ is the temperature of the gas estimated from Fig. 5 in Ressler et al. 2020 [48] as

$$T(r) = 1.5 \times 10^7 \text{ K} \left(\frac{r}{0.4\text{pc}} \right)^{-1}. \tag{4.9}$$

We see that the pressure of CRs becomes relevant at $r \sim 0.07$ pc, around the inner boundary of the region where the accreted gas is fed by the Wolf-Rayet winds ($\sim 0.1 - 1$ pc). The fact that P_{CR} and P_{gas} are comparable at $r \sim 0.07$ may modify somewhat the evolution of the accreting gas near the feeding region. However, regarding the hydrodynamic properties of the gas, we use the fact that P_{CR} should only change the gas pressure by a factor ~ 2 near $r \sim 0.07$ pc, and thus assume that the gas dynamics at those radii is fairly well described by hydrodynamic considerations.

Chapter 5

Conclusions

The spatial distribution of the diffuse gamma-ray emission detected in the CMZ (corresponding to the inner $\sim$ 100 parsecs of the Milky Way), along with its extended spectrum reaching $\sim$ 100 TeV energies, have suggested the presence of a ´PeVatron´, i.e., a cosmic ray (CR) accelerator capable to reach PeV energies, located in the inner part of the GC region. In addition, due to the apparently coincident position of the point-like gamma-ray source HESS J1745-290 with the supermassive black hole Sgr A*, it is suggestive to associate this PeVatron precisely with Sgr A* and the point-like source. This association, however, is challenged by the fact that the point-like source shows a spectral break at a few TeV, not shown by the diffuse emission in the CMZ. In order to reconcile these two spectra, we propose a model in which CRs are continuously injected around Sgr A*, diffusing through the accretion flow and subsequently propagating through the CMZ, emitting very-high energy gamma-rays in both regions, via the decay of neutral pions produced by inelastic hadronic collisions between the CR protons and the background protons.

In this investigations we develop a model for the point-like gamma-ray source HESS J1745-290, considering that it is produced by VHE cosmic-rays injected in the vicinity of the supermassive black hole Sgr A*. Based on certain assumptions for Sgr A* accretion flow (magnetic field and gas density profile, constrained by X-ray observations [11]), we estimate the CR density distribution solving the respective transport equation (Eqs. 2.7, 2.8), and then we calculate the gamma ray emission, produced by the decay of neutral pions subsequently produced by the inelastic collision between the CRs and the background protons of the accretion flow.

In the accretion flow, our model considers the existence of two CR diffusion regimes, which, according to theoretical results and test particle simulation results, depend on the ratio between the Larmor radius of the CRs and the coherence length of the magnetic turbulence, assumed to be isotropic and with a Kolmogorov power-spectrum. In our model, the transition between these two regimes explains the existence of a break in the point-like source spectrum. This transition does not occur for CRs diffusing in the CMZ, explaining the absence of a break in its spectrum. The values obtained for the free parameters of our model that characterize the injection of CRs, and their propagation through the magnetic turbulence present in the accretion flow are consistent with expectations from the observations of the CMZ diffuse

emission and with hydrodynamical and MHD simulations of the Sgr A* accretion flow. On the other hand, our model requires the (very uncertain) coherence length l_c of the magnetic turbulence to have a small, approximately homogeneous value $l_c \sim 10^{14}$ cm $\approx 3 \times 10^{-5}$ pc.

Our results, therefore, support the hypothesis that Sgr A* is capable of accelerating CRs up to a few PeV, contributing to explain the origin of galactic CRs.

An interesting prediction to note in our investigation, is that our model suggests for the point-like source an emission spectrum corresponding to a broken power-law as opposed to a single power-law with exponential cut-off, as has been suggested by other models. This means that, at gamma-ray energies of $\sim$ 10 TeV, the spectrum proposed in our model becomes notably different from other competing models. This is particularly interesting given the advent of CTAO, which will possess a sensitivity about 10 times larger than HESS, reducing the error bars in the observations and thus allowing, in principle, to discriminate between the different models.

Further model discrimination can be done using the possible time variability of HESS J1745-290. This is interesting given the significant variability exhibited by Sgr A* at various wavelengths, characterized by the appearance of prominent "flares", whose timescales are typically close to 1 hour for X-ray and near-infrared emission and 10 hours for submillimeter/radio emission [63]. To date, however, observations have failed to detect variability of the HESS J1745-290 gamma-ray point source [7]. This may be because current observatories do not possess the required sensitivity to detect such variability. In this respect, the upcoming CTAO, will, in principle, have enough sensitivity to detect the point-like source variability. This improvement in observation capabilities represents a great opportunity to extend our study by adding variability to our emission model, which, in a first approximation, would only consider random increases of CRs injected in the vicinity of Sgr A* at different energies. We defer this aspect of our investigation to future research.

Bibliography

[1] Abdalla, H. et al. The H.E.S.S. Galactic plane survey. *Astronomy & Astrophysics*, 612:A1, Apr 2018.

[2] Abramowski, A. et al. Acceleration of petaelectronvolt protons in the galactic centre. *Nature*, 531(7595):476–479, Mar 2016.

[3] Acharya, B. S. et al. *Science with the Cherenkov Telescope Array*. WORLD SCIENTIFIC, 2019.

[4] Adams, C.B. et al. VERITAS Observations of the Galactic Center Region at Multi-TeV Gamma-Ray Energies. *The Astrophysical Journal*, 913(2):115, Jun 2021.

[5] Felix Aharonian. *Very high energy cosmic gamma radiation : a crucial window on the extreme Universe*. WORLD SCIENTIFIC, 2004.

[6] Aharonian, F. et al. Very high energy gamma rays from the direction of Sagittarius A*. *A&A*, 425(1):L13–L17, 2004.

[7] Aharonian, F. et al. Spectrum and variability of the Galactic center VHE gamma-ray source HESS J1745–290. *A&A*, 503(3):817–825, 2009.

[8] Aharonian, F. et al. Massive stars as major factories of Galactic cosmic rays. *Nature Astronomy*, 3:561–567, Mar 2019.

[9] Aharonian, F. and Neronov, A. TeV Gamma Rays From the Galactic Center Direct and Indirect Links to the Massive Black Hole in Sgr A*. *Astrophys Space Sci*, 300:255–265, 2005.

[10] Aloisio, R., Berezinsky, V., and Gazizov, A. The problem of superluminal diffusion of relativistic particles and its phenomenological solution. *The Astrophysical Journal*, 693(2):1275–1282, Mar 2009.

[11] F. K. Baganoff, Y. Maeda, M. Morris, M. W. Bautz, W. N. Brandt, W. Cui, J. P. Doty, E. D. Feigelson, G. P. Garmire, S. H. Pravdo, G. R. Ricker, and L. K. Townsley. Chandra X-Ray Spectroscopic Imaging of Sagittarius A* and the Central Parsec of the Galaxy. *The Astrophysical Journal*, 591(2):891, jul 2003.

[12] Ball, D., Sironi, L., and Özel, F. Electron and proton acceleration in trans-relativistic magnetic reconnection: Dependence on plasma beta and magnetization. *The Astrophysical Journal*, 862(1):80, Jul 2018.

[13] Bednarek, W. and Sobczak, T. Gamma-rays from millisecond pulsar population within the central stellar cluster in the Galactic Centre. *Monthly Notices of the Royal Astronomical Society: Letters*, 435(1):L14–L18, 08 2013.

[14] Belikov, A. et al. Study of the gamma-ray spectrum from the Galactic Center in view of multi-TeV dark matter candidates. *Physical Review D*, 86(8), Oct 2012.

[15] Bernlöhr, K. et al. Monte Carlo design studies for the Cherenkov Telescope Array. *Astroparticle Physics*, 43:171–188, Mar 2013.

[16] Bower, G. et al. ALMA observations of the terahertz spectrum of Sagittarius A*. *The Astrophysical Journal*, 881(1):L2, Aug 2019.

[17] Chael, A. et al. The role of electron heating physics in images and variability of the Galactic Centre black hole Sagittarius A*. *Monthly Notices of the Royal Astronomical Society*, 478(4):5209–5229, Jun 2018.

[18] Chernyakova. A et al. The high-energy, arcminute-scale Galactic Center gamma-ray source. *The Astrophysical Journal*, 726(2), Dec 2010.

[19] HESS Collaboration, Acero, F., et al. Localizing the VHE γ-ray source at the Galactic Centre. *Monthly Notices of the Royal Astronomical Society*, 402(3):1877–1882, Jan 2010.

[20] Cuadra, J. et al. Galactic Centre stellar winds and Sgr A* accretion. *Monthly Notices of the Royal Astronomical Society*, 366(2):358–372, 02 2006.

[21] Cuadra, J. et al. Variable accretion and emission from the stellar winds in the Galactic Centre. *Monthly Notices of the Royal Astronomical Society*, 383(2):458–466, 12 2007.

[22] de Gouveia Dal Pino, Elisabete, M., and Kowal, Grzegorz. *Particle Acceleration by Magnetic Reconnection*, pages 373 – 398. Springer Berlin Heidelberg, 2015.

[23] Elisabete, M. de Gouveia Dal Pino and Kowal, Grzegorz. Particle acceleration by magnetic reconnection. *Magnetic Fields in Diffuse Media*, page 373–398, Oct 2014.

[24] Dexter, J. et al. An 8h characteristic time-scale in submillimetre light curves of Sagittarius A*. *Monthly Notices of the Royal Astronomical Society*, 442(3):2797–2808, 06 2014.

[25] Evoli, C. et al. Galactic factories of cosmic-ray electrons and positrons, 2020.

[26] Aharonian F. *Very high energy gamma radiation: a crucial window on the extreme universe*, chapter 3. World Scientific Publishing Co. Pte. Ltd., 2004.

[27] Fleishman, Gregory D. and Toptygin, Igor N. *Cosmic electrodynamics, Electrodynamics and Magnetic Hydrodynamics of Cosmic Plasmas*, chapter 7.2. Springer., 2013.

[28] Funk, S. and Hinton, J. A. Simulation studies of the high-energy component of a future imaging Cherenkov Telescope Array. *AIP Conference Proceedings*, 1085(1):882–885, 2008.

[29] Ghez, A. M. et al. High Proper-Motion Stars in the Vicinity of Sagittarius A*: Evidence for a Supermassive Black Hole at the Center of Our Galaxy. *The Astrophysical Journal*, 509(2):678–686, Dec 1998.

[30] S. Gillessen, P. M. Plewa, F. Widmann, S. von Fellenberg, M. Schartmann, M. Habibi, A. Jimenez Rosales, M. Bauböck, J. Dexter, F. Gao, I. Waisberg, F. Eisenhauer, O. Pfuhl, T. Ott, A. Burkert, P. T. de Zeeuw, and R. Genzel. Detection of a Drag Force in G2's Orbit: Measuring the Density of the Accretion Flow onto Sgr A* at 1000 Schwarzschild Radii. *The Astrophysical Journal*, 871(1):126, jan 2019.

[31] Yi-Qing Guo et al. The galactic center: A petaelectronvolt cosmic-ray acceleration factory. *The Astrophysical Journal*, 836(2):233, Feb 2017.

[32] Dan Hooper. TASI Lectures on Indirect Searches For Dark Matter. *PoS*, TASI2018:010, 2019.

[33] Huang, Yan et al. Secondary-electron radiation accompanying hadronic GeV–TeV gamma-rays from supernova remnants. *Monthly Notices of the Royal Astronomical Society*, 492(3):4246–4253, 01 2020.

[34] Huentemeyer, P. et al. The Southern Wide-Field Gamma-Ray Observatory (SWGO): A Next-Generation Ground-Based Survey Instrument. In *Bulletin of the American Astronomical Society*, volume 51, page 109, September 2019.

[35] Jokipii, J.R. Cosmic-Ray Propagation. I. Charged Particles in a Random Magnetic Field. *apj*, 146:480, November 1966.

[36] Kelner, S. R., Aharonian, F. A., and Bugayov, V. V. Energy spectra of gamma rays, electrons, and neutrinos produced at proton-proton interactions in the very high energy regime. *Phys. Rev. D*, 74:034018, Aug 2006.

[37] Klepser, S. The MAGIC Telescopes - Status and Recent Results. *arXiv: High Energy Astrophysical Phenomena*, 2011.

[38] LaRosa, T. N., Kassim Namir, E., Joseph, T., Lazio, W., and Hyman, S. D. A wide-field 90 centimeter vla image of the galactic center region. *The Astronomical Journal*, 119(1):207, Jan 2000.

[39] Zhiyuan Li, Morris, Mark R., and Baganoff, Frederick K. Evidence for a parsec-scale jet from the galactic center black hole: interaction with local gas. *The Astrophysical Journal*, 779(2):154, Dec 2013.

[40] Ruo-Yu Liu et al. Modeling the gamma-ray emission in the galactic center with fading cosmic ray accelerator. *The Astrophysical Journal*, 833(2):200, Dec 2016.

[41] Marrone, D. P., Moran, J. M., Jun-Hui Zhao, and Ramprasad Rao. An Unambiguous Detection of Faraday Rotation in Sagittarius A*. *The Astrophysical Journal*, 654(1):L57, dec 2006.

[42] Matthaeus, W. H., Qin, G., Bieber, J. W., and Zank, G. P. Nonlinear collisionless perpendicular diffusion of charged particles. *The Astrophysical Journal*, 590(1):L53, May 2003.

[43] Philipp Mertsch. Test particle simulations of cosmic rays. *Astrophysics and Space Science*, 365(8), Aug 2020.

[44] Masaki Mori et al. The CANGAROO-III project. *AIP Conf. Proc.*, 515(1):485 – 491, 2000.

[45] M. U. Nisa. Probing cosmic-ray propagation with tev gamma rays from the sun using the hawc observatory. *arXiv: High Energy Astrophysical Phenomena*, 2017.

[46] Pierre, M., Siegal-Gaskins, J. M., and Scott, P. Sensitivity of CTA to dark matter signals from the Galactic Center. *Journal of Cosmology and Astroparticle Physics*, 2014(06):024–024, Jun 2014.

[47] Porter, T. A. et al. Galactic pevatrons and helping to find them: Effects of galactic absorption on the observed spectra of very high energy gamma-ray sources. *Phys. Rev. D*, 98:041302, Aug 2018.

[48] Ressler, S. et al. Ab Initio Horizon-scale Simulations of Magnetically Arrested Accretion in Sagittarius A* Fed by Stellar Winds. *The Astrophysical Journal*, 896(1):L6, Jun 2020.

[49] Ressler, S. M., Quataert, E., and Stone, J. M. Hydrodynamic simulations of the inner accretion flow of Sagittarius A* fuelled by stellar winds. *Monthly Notices of the Royal Astronomical Society*, 478(3):3544–3563, May 2018.

[50] Richards, G. . Highlights of Galactic Physics with VERITAS. 2019.

[51] Rodríguez-Ramírez, J. C. et al. Very-high-energy Emission from Magnetic Reconnection in the Radiative-inefficient Accretion Flow of Sgr A *. *The Astrophysical Journal*, 879(1):6, Jun 2019.

[52] Scherer, A., Cuadra, J., and Bauer, Franz E. Galactic center gamma-ray production by cosmic rays from stellar winds and Sgr A East. *Astronomy and Astrophysics*, 659, Mar 2022.

[53] Shalchi, A. *Nonlinear Cosmic Ray Diffusion Theories*. Springer Berlin, Heidelberg, 2009.

[54] Shcherbakov, Roman V. and Baganoff, Frederick K. Inflow-outflow model with conductionand self-consistent feeding for Sgr A*. *The Astrophysical Journal*, 716(1):504, may 2010.

[55] Julian Sitarek. Tev instrumentation: Current and future. *Galaxies*, 10(1), 2022.

[56] Strong, Andrew W., Moskalenko, Igor V., and Ptuskin, Vladimir S. Cosmic-ray propagation and interactions in the galaxy. *Annual Review of Nuclear and Particle Science*, 57(1):285–327, Nov 2007.

[57] Subedi, P. et al. Charged particle diffusion in isotropic random magnetic fields. *The Astrophysical Journal*, 837(2):140, Mar 2017.

[58] Syrovatskii, S. I. The distribution of relativistic electrons in the galaxy and the spectrum of synchrotron radio emission. *Astronomicheskii Zhurnal*, 36:17, 1959.

[59] The CTA Consortium. The Cherenkov Telescope Array Science Goals and Current Status. *EPJ Web Conf.*, 209:01038, 2019.

[60] Ken'ichi Tsuchiya. Detection of Sub-TeV gamma-rays from the Galactic Center with the CANGAROO-II telescope. In *High Energy Gamma-Ray Astronomy*, volume 745 of *American Institute of Physics Conference Series*, pages 403–408, February 2005.

[61] Van Eldik, C. Gamma rays from the galactic centre region: A review. *Astroparticle Physics*, 71:45–70, 2015.

[62] Wang, Q. D. et al. G359.95-0.04: an energetic pulsar candidate near Sgr A*. *Monthly Notices of the Royal Astronomical Society*, 367(3):937–944, Apr 2006.

[63] Witzel, G. et al. Rapid Variability of Sgr A* across the Electromagnetic Spectrum. *The Astrophysical Journal*, 917(2):73, aug 2021.

[64] Huirong Yan. Cosmic Ray Transport in Turbulent Magnetic Field. In *Magnetic Fields in Diffuse Media*, volume 407 of *Astrophysics and Space Science Library*, page 253, January 2015.